IEEE Transactions on Robotics (T-RO) paper, presented at ICRA 2026, Vienna, Austria. Cite as T-RO paper.

Torque-Bounded Task-Space Admittance Control for Redundant Manipulators

Ryo Kikuuwe, *Member, IEEE*

***Abstract*—This article presents a task-space admittance controller applicable to redundant manipulators equipped with torque sensors. It extends Kikuuwe's (2019) torque-bounded admittance controller, which allows for imposing explicit limits on the joint actuator torques without causing unsafe behaviors, such as oscillation and overshoots. The proposed controller enforces that the end-effector follows predefined task-space dynamics as long as the joint torques are unsaturated and the configuration is away from singularities. The behavior in the nullspace, which arises from the redundant degrees of freedom and singular configurations, is governed by predefined joint-space dynamics. The task-space and joint-space dynamics are combined through a newly proposed continualized pseudoinverse, which employs the singular value decomposition. Results of experiments using a seven-degree-of-freedom Kinova Gen3 robot illustrate the validity of the proposed admittance controller in various scenarios, including the case where the robot is fully stretched.**

***Index Terms*—Admittance control, null-space, redundancy, singular configuration.**

I. Introduction

ADMITTANCE control is a control technique to regulate robots' reactions to external forces. It is one form of impedance control and is often referred to as position-based impedance control. A typical implementation of admittance control is illustrated in Fig. 1(a). The admittance controller is composed of an internal position controller and a virtual object referred to as a "proxy," which simulates simple dynamics such as a spring–mass–damper system. The proxy position q_x is adjusted based on the force τ_s measured by a force sensor or a torque sensor and a reference force τ_r provided by a higher level controller. The proxy position q_x acts as the target for the robot's internal position controller, which enforces that the robot's actual position q_s tracks the proxy position q_x. This controller structure is suitable for robots with complicated dynamics because its internal position controller suppresses the influence of the hardware dynamics such as inertia and joint friction. Its applications include haptic interfaces [1], [2], manual guidance of industrial manipulators [3], human–robot collaboration [4], [5], assembly [6], robotic orthoses [7], [8], and surgical robots [9].

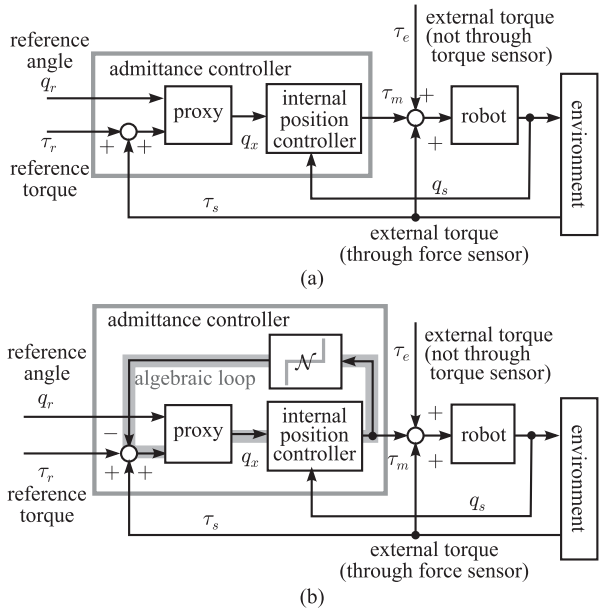

Fig. 1. Systems controlled with admittance controllers. (a) Typical implementation. (b) TBAC [10], on which the proposed method is based. The block $\mathcal{N}$ stands for the normal-cone operator, which is detailed in Sections II-A and III-B.

One concern of the admittance control structure is that it is not straightforward to impose explicit limits on the actuator torques. This is because the torque limits imposed on the internal position controllers can lead to a separation between the proxy position q_x and the actual position q_s, which may result in undesirable snapping-back and overshooting behaviors of the robot. This property poses significant inconvenience in ensuring the safety of admittance-controlled robots in practical applications, especially those involving physical contact with humans.

Another set of technical challenges arises when admittance control should be performed in the task space, i.e., the Cartesian space of the end-effector position and attitude. Such controllers would be needed in, e.g., human–robot collaboration and assembly tasks. In human–robot collaboration, the robot would need to move its end-effector in the direction in which it is pushed or twisted by the human. In assembly tasks, the contact force and compliance should be appropriately regulated in the task space, irrespective of the robot configuration. In this case, one needs to carefully manage the singular configurations and the redundant degrees of freedom (DOFs). When the robot is close to the

Received 8 August 2025; accepted 15 October 2025. Date of publication 6 November 2025; date of current version 24 November 2025. This work was supported by the Kawasaki Heavy Industries, Ltd., Japan. This article was recommended for publication by Associate Editor M. Saveriano and Editor P. M. Wensing upon evaluation of the reviewers' comments.

The author is with the Machinery Dynamics Laboratory, Hiroshima University, Hiroshima 739-8527, Japan (e-mail: kikuuwe@ieee.org).

This article has a supplementary multimedia attachment; an MP4 movie clip illustrating the experiments in Section VI. The file is 23 MB in size.

This article has supplementary downloadable material available at https://doi.org/10.1109/TRO.2025.3629785, provided by the author.

Digital Object Identifier 10.1109/TRO.2025.3629785

IEEE Transactions on Robotics (T-RO) paper, presented at ICRA 2026, Vienna, Austria. Cite as T-RO paper.

singular configuration, the proxy velocity in the task space may be mapped to an excessively large joint velocity, which results in unsafe behavior of the robot. The singular configurations have been mainly handled by avoiding them by additional control algorithms [11], [12], or by using approximate pseudoinverses of Jacobians [13], [14]. Such approximations, however, would result in a certain level of inaccuracy in the task-space motion, as discussed in [13] and [15]. The redundancy has been treated by injecting additional damping [16], [17], [18], [19], [20] and compliance [17], [21], [22] in the nullspace motion.[1]

In a previous paper, Kikuuwe [10] proposed a controller named a torque-bounded admittance control (TBAC), which incorporates explicit torque limit to the internal position controller while maintaining the consistency between the proxy position and the actual position. It acts as a standard admittance controller as long as the actuator torque is not saturated, but once it is saturated, the controller yields to external forces without inducing overshoot or oscillations. The controller incorporates an algebraic loop, as illustrated in Fig. 1(b), which algebraically constrains the proxy position and the actuator torque. The entire controller is formulated as a differential algebraic inclusion (DAI), with a discrete-time implementation derived through the implicit (backward) Euler discretization. This method was originally designed as a 1-D controller and thus can be implemented independently in each joint. That is, it is usable only in the joint space.

This article presents a task-space extension of TBAC that tolerates singular configurations and can be used with redundant manipulators. It imposes explicit torque limits to each joint without impairing the safety, while it enforces that the end-effector follows predefined task-space proxy dynamics as long as the joint torques are unsaturated and the robot is out of the singularity configurations. The dynamics of the robot in the nullspace is determined by predetermined joint-space proxy dynamics. The task- and joint-space dynamics are combined as a lexicographic minimization problem, and its computational implementation is realized with an alternative approximation of the pseudoinverse, which is named a continualized pseudoinverse. The continualized pseudoinverse is continuous with respect to the singular values while it is equal to the original pseudoinverse as long as the singular values are zero or larger than a predetermined threshold. The controller was validated with experiments using a seven-DOF Kinova Gen3 robot, in which the controller is shown to tolerate singular configurations, such as those where the manipulator is fully stretched.

One feature of the proposed controller is its incorporation of full admittance (inertia, viscosity, and stiffness) in both the task space and the joint space, unlike the methods in [16], [18], [19], [20], and [22]. Another feature is that it realizes the nullspace admittance control without explicitly computing the nullspace basis or the nullspace velocities, in contrast to the approach in [17], [20], and [23]. It may also be an important point that the proposed controller employs concise representations of the task-space dynamics involving rotations with a newly defined time-derivative operator for quaternions. The operator allows for the backward-Euler discretization of differential equations involving quaternions and angular velocity vectors, as detailed in Appendix A. In addition to the above-mentioned features, the proposed controller inherits the main feature of TBAC, which is the safety under the actuator torque saturation.

The rest of this article is organized as follows. Section II shows some mathematical preliminaries. Section III provides an overview and reinterpretation of the previously proposed 1-D TBAC [10]. Section IV proposes a new admittance controller. Section V provides some theoretical analyses. Section VI shows the results of experiments employing a seven-DOF manipulator. Finally, Section VII concludes this article.

II. Mathematical Preliminaries

A. Notations

In this article, $\mathbb{R}$ denotes the set of all real numbers, and $\mathbb{H}$ denotes the set of all unit quaternions. This article treats a quaternion as a 4-D vector, which means that $\mathbb{H} \subset \mathbb{R}^4$. We also use $\mathbb{P} = \mathbb{R}^3 \times \mathbb{H} \subset \mathbb{R}^7$, which is used to express the position and the attitude of the end-effector by a 7-D single vector. We use the addition operator $\oplus$, the subtraction operator $\ominus$, and the time-derivative operator $\circ$ for $\mathbb{P}$, which are defined in Appendix A.

This article uses the following function:

$$\mathrm{proj}_{\mathcal{C}}(\boldsymbol{x}) \triangleq \operatorname*{argmin}_{\boldsymbol{\xi}\in\mathcal{C}} \|\boldsymbol{\xi} - \boldsymbol{x}\| \tag{1}$$

where $\mathcal{C} \subset \mathbb{R}^n$ is a convex set. Here, $\operatorname{argmin}_{\boldsymbol{x}\in\mathcal{C}} f(\boldsymbol{x})$ denotes the value of $\boldsymbol{x} \in \mathcal{C}$ that minimizes $f(\boldsymbol{x})$, which is single-valued (i.e., unique) if the set $\mathcal{C}$ is convex. The function $\mathrm{proj}_{\mathcal{C}}$ can be said to be a projection operator onto the set $\mathcal{C}$. This article also uses the notation $\mathrm{co}\,\mathcal{C}$ to denote the convex hull of a set $\mathcal{C}$. With two scalars A and B, $\mathrm{co}\{A, B\} = \mathrm{co}\{B, A\} = [\min(A, B), \max(A, B)]$.

We also use the function $\mathrm{sat}_1 : \mathbb{R}^n \times \mathbb{R}^n \to \mathbb{R}^n$ and the function $\mathrm{sat}_3 : \mathbb{R}^2 \times \mathbb{R}^6 \to \mathbb{R}^6$, which are respectively defined as follows:

$$\mathrm{sat}_1(\boldsymbol{F}, \boldsymbol{x}) \triangleq \begin{bmatrix} F_1 x_1 / \max(F_1, |x_1|) \\ \vdots \\ F_n x_n / \max(F_n, |x_n|) \end{bmatrix} \tag{2}$$

$$\mathrm{sat}_3(\boldsymbol{F}, \boldsymbol{x}) \triangleq \begin{bmatrix} F_1 \boldsymbol{x}_{1:3} / \max(F_1, \|\boldsymbol{x}_{1:3}\|) \\ F_2 \boldsymbol{x}_{4:6} / \max(F_2, \|\boldsymbol{x}_{4:6}\|) \end{bmatrix} \tag{3}$$

where F_i and x_i stands for the ith elements of $\boldsymbol{F}$ and $\boldsymbol{x}$, respectively, and $\boldsymbol{x}_{i:j}$ stands for the $(j - i + 1)$-dimensional vector composed of the ith to jth elements of $\boldsymbol{x}$. The function sat_1 is for saturating the torque values of n joints, and sat_3 is for saturating the translational and rotational subvectors of the 6-D force/torque vectors.

This article uses the "argument of the lexicographic minimum" operator, which should be read as follows:

$$\operatorname*{arglexmin}_{\boldsymbol{x}\in\mathcal{C}} \{f(\boldsymbol{x}), g(\boldsymbol{x})\} = \operatorname*{argmin}_{\boldsymbol{x}\in\operatorname{argmin}_{x\in\mathcal{C}} f(\boldsymbol{x})} g(\boldsymbol{x}). \tag{4}$$

[1] This article uses the term "nullspace" to mean the set of joint-space velocities that do not affect the end-effector velocity.

This operator provides the value of $\boldsymbol{x}$ that minimizes $f(\boldsymbol{x})$ at the first priority and also $g(\boldsymbol{x})$ at the second priority. That is, it returns the value of $\boldsymbol{x}$ that minimizes $g(\boldsymbol{x})$ among the values of $\boldsymbol{x}$ that minimize $f(\boldsymbol{x})$. The operator arglexmin can inherently be set-valued, but this article only deals with cases where it is single-valued.

With a symmetric positive-semidefinite matrix $\boldsymbol{A}$, we use $\boldsymbol{A}^h$ to mean an arbitrary square matrix that satisfies $\boldsymbol{A} = \boldsymbol{A}^h \boldsymbol{A}^{hT}$ where $\boldsymbol{A}^{hT} \triangleq (\boldsymbol{A}^h)^T$. A matrix $\boldsymbol{A}^h$ can be the principal (symmetric) square root matrix $\boldsymbol{A}^{1/2}$ if all elements of $\boldsymbol{A}$ have the same physical dimensions. We use $\boldsymbol{A}^h$ to preserve the physical consistency because $\boldsymbol{A}$ comprising elements with different physical dimensions may result in $\boldsymbol{A}^{1/2}$ whose nondiagonal elements do not have consistent physical dimensions. If $\boldsymbol{A}^{-1}$ exists, one has $\boldsymbol{A}^{-1} = \boldsymbol{A}^{-hT}\boldsymbol{A}^{-h}$ where $\boldsymbol{A}^{-hT} \triangleq (\boldsymbol{A}^{hT})^{-1}$ and $\boldsymbol{A}^{-h} \triangleq (\boldsymbol{A}^h)^{-1}$. With such a matrix $\boldsymbol{A}^h$, the following relation holds:

$$\|\boldsymbol{x}\|_{\boldsymbol{A}} = \sqrt{\boldsymbol{x}^T \boldsymbol{A}\boldsymbol{x}} = \|\boldsymbol{A}^{hT}\boldsymbol{x}\| \tag{5}$$

which means that a weighted vector norm can be rewritten as an unweighted norm using $\boldsymbol{A}^{hT}$.

Derivations in Section III-B utilize some set-valued expressions. Addition and subtraction between a set $\mathcal{B} \subset \mathbb{R}$ and a single value $x \in \mathbb{R}$ should be understood as

$$\mathcal{B} \pm x = \bigcup_{\eta \in \mathcal{B}} (\eta \pm x). \tag{6}$$

This implies that, if $\mathcal{B} = [A, B] \subset \mathbb{R}$, $\mathcal{B} + x = [A + x, B + x]$. We use a normal-cone operator [10], which is the set-valued function defined as follows:

$$\mathcal{N}_{[A,B]}(x) = \begin{cases} \emptyset & \text{if } x > B \ \wedge \ x < A \\ [0, \infty) & \text{if } x = B \neq A \\ 0 & \text{if } A < x < B \\ (-\infty, 0] & \text{if } x = A \neq B \\ (-\infty, \infty) & \text{if } x = A = B \end{cases} \tag{7}$$

where $A \leq B$. The original definition of the normal-cone operator, which is for closed convex sets in the multidimensional vector space, can be found in the literature, e.g., [24, Section 2.2][25, Definition B.5][26, Definition 2]. The definition (7) is the special case for closed intervals in the 1-D space. The following algebraic equivalence holds between the normal cone and the projection operator:

$$x + \mathcal{N}_{[A,B]}(x) \ni y \iff x = \mathrm{proj}_{[A,B]}(y). \tag{8}$$

A proof of (8) is provided in [24, Section A.3]. It is used for converting a set-valued expression into an ordinary (single-valued) expression in Section III-B.

B. Pseudoinverse and Lexicographic Minimization

Recall that, for a matrix $\boldsymbol{A} \in \mathbb{R}^{m \times n}$, there always exists a matrix $\boldsymbol{A}^+ \in \mathbb{R}^{n \times m}$ that satisfies the following conditions:

$$\boldsymbol{A}\boldsymbol{A}^+\boldsymbol{A} = \boldsymbol{A}, \quad \boldsymbol{A}^+\boldsymbol{A}\boldsymbol{A}^+ = \boldsymbol{A}^+$$
$$(\boldsymbol{A}\boldsymbol{A}^+)^T = \boldsymbol{A}\boldsymbol{A}^+, \quad (\boldsymbol{A}^+\boldsymbol{A})^T = \boldsymbol{A}^+\boldsymbol{A}. \tag{9}$$

The matrix $\boldsymbol{A}^+$ is referred to as the pseudoinverse of $\boldsymbol{A}$.

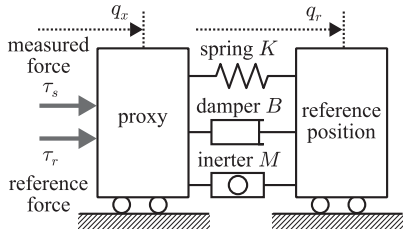

Fig. 2. Physical interpretation of the proxy.

This article uses the following fact.

Theorem 1: With $\boldsymbol{A} \in \mathbb{R}^{m \times n}$ and $\boldsymbol{b} \in \mathbb{R}^m$, the following statement holds true:

$$\underset{\boldsymbol{x} \in \mathbb{R}^n}{\mathrm{arglexmin}} \{\|\boldsymbol{A}\boldsymbol{x} - \boldsymbol{b}\|^2, \|\boldsymbol{x}\|^2\} = \boldsymbol{A}^+\boldsymbol{b}. \tag{10}$$

The proof is given in Appendix B. The author does not consider it a new result, but the expression (10), in its concise form, cannot be found in the literature as far as the author is aware.

As an extension of Theorem 1, we have the following.

Corollary 1: The following statement holds true:

$$\underset{\boldsymbol{x} \in \mathbb{R}^n}{\mathrm{arglexmin}} \{\|\boldsymbol{A}\boldsymbol{x} - \boldsymbol{b}\|^2, \|\boldsymbol{C}\boldsymbol{x} - \boldsymbol{d}\|^2\}$$
$$= \boldsymbol{C}^{-1}\bar{\boldsymbol{A}}^+\boldsymbol{b} + \boldsymbol{C}^{-1}(\boldsymbol{I}_n - \bar{\boldsymbol{A}}^+\bar{\boldsymbol{A}})\boldsymbol{d} \tag{11}$$

where $\bar{\boldsymbol{A}} \triangleq \boldsymbol{A}\boldsymbol{C}^{-1} \in \mathbb{R}^{m \times n}$, $\boldsymbol{A} \in \mathbb{R}^{m \times n}$, $\boldsymbol{b} \in \mathbb{R}^m$, $\boldsymbol{d} \in \mathbb{R}^n$, and $\boldsymbol{C} \in \mathbb{R}^{n \times n}$ is a regular matrix.

Its proof is also given in Appendix B.

III. Overview and Reinterpretation of TBAC

In a previous paper, Kikuuwe [10] proposed a controller referred to as a TBAC. The controller in [10] is a 1-D controller and was validated only through joint-space experiments, where the controller was implemented independently to each joint of a robot. This section provides a quick overview of TBAC from a somewhat different perspective.

A. Conventional Admittance Control

Here we consider a one-DOF robot with a single actuated joint equipped with a joint position (angle) sensor and a force (torque) sensor. Let $q_s \in \mathbb{R}$ denote the measured position, $\tau_m \in \mathbb{R}$ denote the commanded actuator force, and $\tau_s \in \mathbb{R}$ be the measured external force.

A typical and conventional idea of admittance control is that the robot should be position-controlled to follow a virtual object, hereinafter referred to as a proxy, such as those illustrated in Fig. 2. The proxy in Fig. 2 is an inerter–damper–spring[2] system, of which the position is $q_x \in \mathbb{R}$, connected to a reference position $q_r \in \mathbb{R}$ and subject to the measured force τ_s and a reference force $\tau_r \in \mathbb{R}$. The motion of this proxy is governed by the following

[2]An inerter is a mechanical element that produces the force proportional to the acceleration difference between its two ends, such as those appearing in [27].

IEEE Transactions on Robotics (T-RO) paper, presented at ICRA 2026, Vienna, Austria. Cite as T-RO paper.

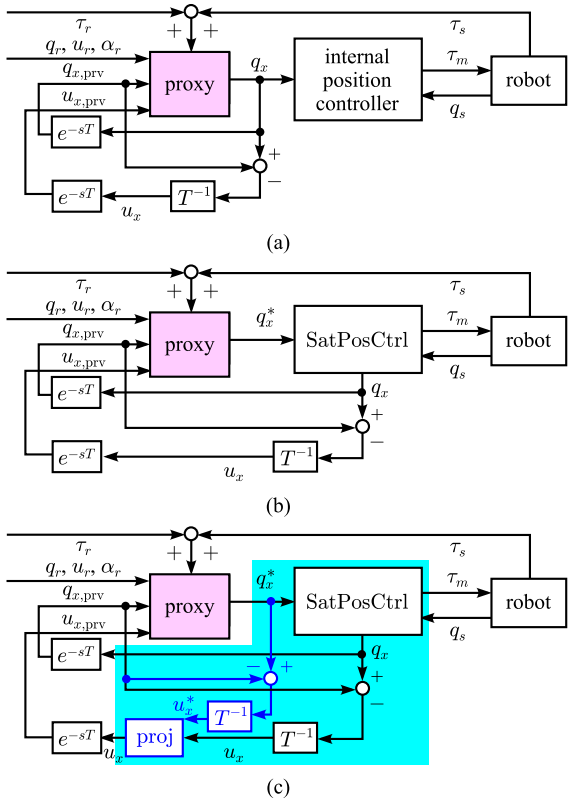

Fig. 3. Alternative representations of admittance controllers. (a) Typical conventional admittance controller. (b) Basic version of TBAC [10, Sec. III]. (c) Velocity-projecting version of TBAC [10, Sec. V.B]. The function SatPosCtrl is defined in (16). For simplicity, the error integral b_{xs} is omitted here.

equation of motion:

$$M(\ddot{q}_x - \alpha_r) + B(\dot{q}_x - u_r) + K(q_x - q_r) = \tau_s + \tau_r \tag{12}$$

where $\alpha_r \triangleq \dot{u}_r$ and $u_r \triangleq \dot{q}_r$. Here, $M > 0$ is the inertia of the inerter, $B > 0$ is the viscosity of the damper, and $K > 0$ is the stiffness of the spring. When the robot is in contact with an environment surface, the force from the environment to the robot is measured as the force τ_s, which acts on the proxy through (12). When the robot is statically in contact with an environment surface, $\tau_s + \tau_r = K(q_x - q_r)$ holds true. This means that, if the spring constant K is set to be zero, $-\tau_r$ can be interpreted as the desired value of τ_s, and the right-hand side of (12) can be interpreted as the error between the actual force τ_s and the desired force $-\tau_r$.

The proxy position q_x and velocity $\dot{q}_x$ are updated according to (12), and the position q_x is used as the command position to the position controller, which can be typically written as follows:

$$\tau_m = K_c(q_x - q_s) + B_c(\dot{q}_x - \dot{q}_s) + L_c \int (q_x - q_s)dt \tag{13}$$

where K_c, B_c, and L_c are the proportional, derivative, and integral gains. A typical algorithmic structure of an admittance controller can be illustrated in Fig. 3(a). Here, T is the sampling interval and the subscript prv indicates the value of the associated variable in the previous timestep. Based on the Euler discretization, we have $q_x = q_{x,\mathrm{prv}} + Tu_x$ where $u_x \triangleq \dot{q}_x$. In the structure of Fig. 3(a), the proxy position q_x is sent to the position controller. The proxy position q_x and velocity u_x are reused in the next timestep to update them to new values.

B. Basic Version of TBAC

Let us consider the case where we need to impose the constraint $\tau_m \in [-F_c, F_c]$ on the actuator torque τ_m where $F_c > 0$. The TBAC [10] is a controller to deal with such a case, and it is described as follows:

$$M(\ddot{q}_x - \alpha_r) + B(\dot{q}_x - u_r) + K(q_x - q_r) \in \tau_s + \tau_r - \mathcal{N}_{[-F_c,F_c]}(\tau_m) \tag{14a}$$

$$\tau_m = K_c(q_x - q_s) + B_c(\dot{q}_x - \dot{q}_s) + L_c \int (q_x - q_s)dt. \tag{14b}$$

This set of equations can be seen as a DAI with respect to q_x. Because the normal-cone term $+\mathcal{N}_{[-F_c,F_c]}(\tau_m)$ in (14a) forbids τ larger than F_c, the proxy's acceleration $\ddot{q}_x$ is determined so that $|\tau| \le F_c$ is satisfied. As long as $|\tau| < F_c$, the controller (14) is equivalent to the ordinary admittance controller described by (12) and (13). The structure of TBAC (14) is shown in Fig. 1(b), in which the term $\mathcal{N}_{[-F_c,F_c]}(\tau_m)$ in (14a) appears as an algebraic feedback loop.

The discrete-time representation of the controller (14) can be obtained by its implicit Euler discretization, which can be derived by replacing the derivatives by the finite differences, e.g., $\dot{u}_x := (u_x - u_{x,\mathrm{prv}})/T$. Through some derivations detailed in [10], which include the use of (8) to treat the set-valuedness, the discrete-time algorithm for solving (14) can be given as follows:

$$\hat{\tau}_s := \tau_s + \tau_r + M\alpha_r + Bu_r + K(q_r - q_{x,\mathrm{prv}}) \tag{15a}$$

$$q_x^* := \frac{Mu_{x,\mathrm{prv}} + T\hat{\tau}_s}{M + BT + KT^2} \tag{15b}$$

$$\{\tau_m, q_x\} := \mathrm{SatPosCtrl}(q_x^*, q_{x,\mathrm{prv}}, q_s, u_s, b_{xs,\mathrm{prv}}) \tag{15c}$$

$$u_x = (q_x - q_{x,\mathrm{prv}})/T \tag{15d}$$

$$b_{xs} := b_{xs,\mathrm{prv}} + T(q_x - q_s) \tag{15e}$$

where the function SatPosCtrl, which is a "saturated position controller," is defined as follows:

$$\text{Function SatPosCtrl}(q_x^*, q_{x,\mathrm{prv}}, q_s, u_s, b_{xs,\mathrm{prv}}) \tag{16a}$$

$$\tau_m^{**} := L_c b_{xs,\mathrm{prv}} - B_c(u_s - (q_s - q_{x,\mathrm{prv}})/T) \tag{16b}$$

$$\tau_m^{*} := (K_c + L_cT)(q_x^* - q_s) + \tau_m^{**} \tag{16c}$$

$$\tau_m := \mathrm{proj}_{[-F_c,F_c]}(\tau_m^*) \tag{16d}$$

$$q_x := q_s + \frac{\tau_m - \tau_m^{**}}{B_c/T + K_c + L_cT} \tag{16e}$$

$$\text{Return } \{\tau_m, q_x\}. \tag{16f}$$

Note that this algorithm (15) does not involve any set-valued functions or nonclosed-form equations, in spite of the fact

that its original continuous-time representation (14) involves set-valuedness and differential–algebraic constraints.

The structure of the algorithm (15) can be illustrated, as in Fig. 3(b). It can be interpreted as a combination of the proxy dynamics, represented by (15a) and (15b), and a saturated position controller, represented by the function SatPosCtrl defined in (16). The quantity q_x^* calculated by (15b) can be seen as a "tentative" proxy position without considering the actuator saturation. This is provided to the function SatPosCtrl, of which the outputs are the necessary torque τ_m and a "corrected" proxy position q_x, which corresponds to the maximal permissible velocity under the torque limitation. If the actuator is not saturated, the tentative proxy position q_x^* is just adopted as the proxy velocity q_x. The corrected proxy position q_x is used in the next timestep.

C. Velocity-Projecting Version of TBAC

The previous paper [10] pointed out a flaw of the algorithm (15), which is that the actuator saturation may inject kinetic energy into the robot. When the robot is accelerated by an external force and the actuator torque is saturated, the proxy velocity u_x is also increased, and it affects the proxy position q_x in the next timestep. This means that, when the actuator is saturated, the work done by the external force is stored as the kinetic energy of the proxy, as well as that of the robot. This feature is undesirable for safety reasons.

To eliminate this flaw, Kikuuwe [10] proposed a velocity projection method, which was referred to as a "Modification B" in [10, Section V.B]. It modifies u_x so that it satisfies $u_x \in \mathrm{co}\{0, u_x^*\}$, which indicates that the saturation only shrinks the proxy velocity u_x^* without altering its direction. This idea can be realized by adding the line

$$u_x := \mathrm{proj}_{\mathrm{co}\{0,u_x^*\}}(u_x) \tag{17}$$

in the end of the algorithm (15). The modified controller (15) + (17), which can be said to be a "velocity-projecting version" of TBAC, is illustrated in Fig. 3(c). It should be emphasized that this modification does not alter the current proxy position q_x, but does modify only the proxy velocity u_x, which influences the proxy position in the next timestep. The underlying idea is that the proxy velocity, which is a state variable independent from the proxy position, does not need to satisfy $u_x = (q_x - q_{x,\mathrm{prv}})/T$, although the proxy position q_x needs to be consistent with the torque τ_m.

IV. Proposed Controller

This section proposes a multidimensional extension of TBAC applicable to redundant manipulators. The overall structure of the controller is illustrated in Fig. 4. The desired dynamics of the robot are defined by two proxies, the task-space proxy and the joint-space proxy. The task-space proxy acts in the task space while the joint-space proxy is effective only in the nullspace. The joint-space proxy is necessary not only to deal with the redundancy, but also to deal with the singular configurations, because even a nonredundant manipulator can have a nullspace when it enters a singular configuration. The block SatPosCtrl in Fig. 4 is an elementwise, multidimensional version of the one defined in (16), which acts on each joint independently. We assume that the robot is equipped with torque sensors attached to the joints.

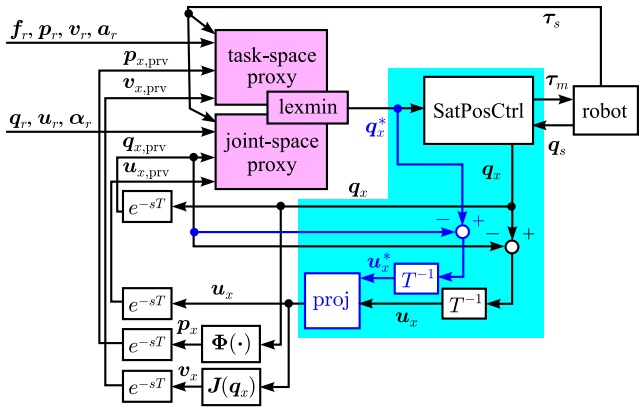

Fig. 4. Proposed controller. Note that the highlighted part has a structure identical to that of Fig. 3(c). The error integral b_{xs} is omitted here for simplicity.

A. Structure

We here consider an n-DOF rigid-link manipulator with a single end-effector. We use $\boldsymbol{q} \in \mathbb{R}^n$, $\boldsymbol{u} \in \mathbb{R}^n$, and $\boldsymbol{\alpha} \in \mathbb{R}^n$ to denote the joint-space position, velocity, and acceleration vectors, respectively, and they satisfy $\boldsymbol{u} = \dot{\boldsymbol{q}}$ and $\boldsymbol{\alpha} = \dot{\boldsymbol{u}}$. We also use $\boldsymbol{p} \in \mathbb{P}$, $\boldsymbol{v} \in \mathbb{R}^6$, and $\boldsymbol{a} \in \mathbb{R}^6$ to denote the task-space position, velocity, and acceleration vectors, respectively. It should be noted that $\boldsymbol{p} \in \mathbb{P}$ is a 7-D vector composed of the 3-D position-vector part and the 4-D attitude-quaternion part. Each of the vectors $\boldsymbol{v} \in \mathbb{R}^6$ and $\boldsymbol{a} \in \mathbb{R}^6$ is composed of a 3-D translational part and a 3-D rotational part. They are associated as $\boldsymbol{v} = \mathring{\boldsymbol{p}}$ and $\boldsymbol{a} = \dot{\boldsymbol{v}}$ where $\circ$ is the time-derivative operator for $\mathbb{P}$ defined in Appendix A. We also use $\boldsymbol{\tau} \in \mathbb{R}^n$ and $\boldsymbol{f} \in \mathbb{R}^6$ to denote a joint torque vector and a task-space force vector, respectively. These symbols may be used with the subscripts s, x, and r, denoting the measured values, the proxy values, and the reference values, respectively.

With the forward kinematics $\boldsymbol{\Phi} : \mathbb{R}^n \to \mathbb{P}$ of the manipulator, we have $\boldsymbol{p} = \boldsymbol{\Phi}(\boldsymbol{q})$, and using the Jacobian matrix $\boldsymbol{J} : \mathbb{R}^n \to \mathbb{R}^6$, we have $\boldsymbol{v} = \boldsymbol{J}(\boldsymbol{q})\boldsymbol{u}$. We also use the Jacobian rate-of-change matrix $\boldsymbol{H} : \mathbb{R}^n \times \mathbb{R}^n \to \mathbb{R}^6$ defined as $\boldsymbol{H}(\boldsymbol{q}, \dot{\boldsymbol{q}}) \triangleq d\boldsymbol{J}(\boldsymbol{q})/dt$, which satisfies $\dot{\boldsymbol{v}} = \boldsymbol{J}(\boldsymbol{q})\dot{\boldsymbol{u}} + \boldsymbol{H}(\boldsymbol{q}, \boldsymbol{u})\boldsymbol{u}$.

As can be seen in Fig. 4, we assume that the manipulator is equipped with joint angle sensors and joint torque sensors, which provide the measured angle vector $\boldsymbol{q}_s \in \mathbb{R}^n$ and the measured torque vector $\boldsymbol{\tau}_s \in \mathbb{R}^n$, respectively. The proposed controller involves two different proxies, which are the task-space proxy and the joint-space proxy. They are governed by certain dynamics coupled with a lexicographic prioritization, indicated as "lexmin" in the figure. The positions and the velocities of the joint-space proxy and the task-space proxy are kept consistent with each other through the relations $\boldsymbol{p}_x = \boldsymbol{\Phi}(\boldsymbol{q}_x)$ and $\boldsymbol{v}_x = \boldsymbol{J}(\boldsymbol{q}_x)\boldsymbol{u}_x$ at every timestep. The output of the controller is the command torque $\boldsymbol{\tau}_m \in \mathbb{R}^6$ sent to the joint actuators.

Recall that the 1-D velocity-projecting version of TBAC is written as (15) + (17). As its direct extension, the algorithm of

IEEE Transactions on Robotics (T-RO) paper, presented at ICRA 2026, Vienna, Austria. Cite as T-RO paper.

the proposed controller is given as follows:

$$\boldsymbol{q}_x^* := \mathrm{TwoProxies}(\boldsymbol{p}_{x,\mathrm{prv}}, \boldsymbol{v}_{x,\mathrm{prv}}, \boldsymbol{q}_{x,\mathrm{prv}}, \boldsymbol{u}_{x,\mathrm{prv}}, \boldsymbol{\tau}_s) \tag{18a}$$

$$\{\boldsymbol{\tau}_m, \boldsymbol{q}_x\} := \mathrm{SatPosCtrl}(\boldsymbol{q}_x^*, \boldsymbol{q}_{x,\mathrm{prv}}, \boldsymbol{q}_s, \boldsymbol{u}_s, \boldsymbol{b}_{xs,\mathrm{prv}}) \tag{18b}$$

$$\boldsymbol{u}_x := (\boldsymbol{q}_x - \boldsymbol{q}_{x,\mathrm{prv}})/T \tag{18c}$$

$$\boldsymbol{b}_{xs} := \boldsymbol{b}_{xs,\mathrm{prv}} + T(\boldsymbol{q}_x - \boldsymbol{q}_s) \tag{18d}$$

$$\boldsymbol{u}_x := \mathrm{proj}_{\mathrm{co}\{\boldsymbol{0}_n, \boldsymbol{u}_x^*\}}(\boldsymbol{u}_x) \tag{18e}$$

$$\boldsymbol{p}_x := \boldsymbol{\Phi}(\boldsymbol{q}_x) \tag{18f}$$

$$\boldsymbol{v}_x := \boldsymbol{J}(\boldsymbol{q}_x)\boldsymbol{u}_x \tag{18g}$$

where the function TwoProxies represents the combined proxy dynamics that will be detailed in the next Section IV-B. It determines the tentative joint-space proxy position $\boldsymbol{q}_x^*$, and it is used as the input to SatPosCtrl, the saturated position controller defined in (16), to obtain the joint torque command $\boldsymbol{\tau}_m$. As has been detailed in Section III-B, the function SatPosCtrl provides the corrected proxy position $\boldsymbol{q}_x$ as another output, and the line (18c) gives the corresponding proxy velocity $\boldsymbol{u}_x$. The velocity is then "projected" in (18e), resulting in a recorrected velocity $\boldsymbol{u}_x$. This projection operation is discussed in Section III-C, and its multidimensional version is given as

$$\mathrm{proj}_{\mathrm{co}\{\boldsymbol{0}_n, \boldsymbol{u}_x^*\}}(\boldsymbol{u}_x) \triangleq \mathrm{proj}_{[0,1]}\left(\frac{\boldsymbol{u}_x^{*T}\boldsymbol{u}_x}{\boldsymbol{u}_x^{*T}\boldsymbol{u}_x^*}\right)\boldsymbol{u}_x^*. \tag{19}$$

Finally, the joint-space proxy position $\boldsymbol{q}_x$ and velocity $\boldsymbol{u}_x$ are converted into the task-space proxy position $\boldsymbol{p}_x$ and velocity $\boldsymbol{v}_x$, respectively, through the forward kinematics.

Note that the lines (18b)–(18e) of the proposed controller exactly correspond to the lines (15c)–(15e) plus (17) of the 1-D TBAC.

B. Combined Proxy Dynamics

Now the combined proxy dynamics, which appear as the function TwoProxies in the line (18a) of the proposed controller (18), is presented. It is composed of the task-space proxy dynamics and the joint-space proxy dynamics. The task-space proxy dynamics is given in the following continuous-time representation:

$$\mathring{\boldsymbol{p}}_x = \boldsymbol{v}_x,\ \dot{\boldsymbol{v}}_x = \boldsymbol{a}_x \tag{20a}$$

$$\begin{aligned}&\boldsymbol{M}_{\mathrm{T}}(\boldsymbol{a}_x - \boldsymbol{a}_r) + \boldsymbol{B}_{\mathrm{T}}(\boldsymbol{v}_x - \boldsymbol{v}_r) + \mathrm{sat}_3(\boldsymbol{F}_{\mathrm{T}}, \boldsymbol{K}_{\mathrm{T}}(\boldsymbol{p}_x \ominus \boldsymbol{p}_r))\\ &\quad = \boldsymbol{f}_s + \boldsymbol{f}_r\end{aligned} \tag{20b}$$

where $\boldsymbol{f}_s$ and $\boldsymbol{f}_r \in \mathbb{R}^6$ are the force acting on the end-effector and the reference force, respectively, and $\boldsymbol{a}_r \triangleq \dot{\boldsymbol{v}}_r$ and $\boldsymbol{v}_r \triangleq \mathring{\boldsymbol{p}}_r$. The matrices $\boldsymbol{M}_{\mathrm{T}}$, $\boldsymbol{B}_{\mathrm{T}}$, and $\boldsymbol{K}_{\mathrm{T}} \in \mathbb{R}^{6\times 6}$ are the inertia, viscosity, and stiffness matrices, respectively, and they are symmetric positive-definite matrices. In the third term of the left-hand side of (20b), the function sat_3, defined in (3), is used to allow for setting upperbounds to the task-space proxy spring force. Here, $\boldsymbol{F}_{\mathrm{T}}$ is a vector composed as $\boldsymbol{F}_{\mathrm{T}} = [F_{\mathrm{tra}}, F_{\mathrm{rot}}]^T \in \mathbb{R}^2$ where F_{tra} and F_{rot} are the limits for the translational and rotational components, respectively. The operator $\ominus$ is the subtraction operator for $\mathbb{P}$, which is defined in Appendix A.

In the dynamics (20), $\boldsymbol{f}_s$ is not directly available. It however can be assumed to satisfy the following relation with the measured torque $\boldsymbol{\tau}_s \in \mathbb{R}^n$:

$$\boldsymbol{\tau}_s \approx \boldsymbol{J}(\boldsymbol{q}_s)^T \boldsymbol{f}_s. \tag{21}$$

A discrete-time approximation of (20) can be given as follows:

$$\boldsymbol{p}_x = \boldsymbol{p}_{x,\mathrm{prv}} \oplus T\boldsymbol{v}_x,\ \boldsymbol{v}_x = \boldsymbol{v}_{x,\mathrm{prv}} + T\boldsymbol{a}_x \tag{22a}$$

$$\begin{aligned}&\boldsymbol{M}_{\mathrm{T}}(\boldsymbol{a}_x - \boldsymbol{a}_r) + \boldsymbol{B}_{\mathrm{T}}(\boldsymbol{v}_{x,\mathrm{prv}} + T\boldsymbol{a}_x - \boldsymbol{v}_r)\\ &\quad + \mathrm{sat}_3(\boldsymbol{F}_{\mathrm{T}}, \boldsymbol{K}_{\mathrm{T}}(\boldsymbol{p}_{x,\mathrm{prv}} \ominus \boldsymbol{p}_r)) = \boldsymbol{f}_s + \boldsymbol{f}_r\end{aligned} \tag{22b}$$

where the operator $\oplus$ is the addition operator between $\mathbb{P}$ and $\mathbb{R}^6$, which is defined in Appendix A. One can rewrite (22b) as follows:

$$\hat{\boldsymbol{C}}_{\mathrm{T}}\boldsymbol{a}_x - \hat{\boldsymbol{b}}_{\mathrm{T}} - \boldsymbol{f}_s = \boldsymbol{0}_6 \tag{23}$$

where

$$\hat{\boldsymbol{C}}_{\mathrm{T}} \triangleq \boldsymbol{M}_{\mathrm{T}} + T\boldsymbol{B}_{\mathrm{T}} \tag{24}$$

$$\hat{\boldsymbol{b}}_{\mathrm{T}} \triangleq -\boldsymbol{B}_{\mathrm{T}}\boldsymbol{v}_{x,\mathrm{prv}} + \boldsymbol{f}_r + \boldsymbol{f}_{re} \tag{25}$$

$$\boldsymbol{f}_{re} \triangleq \boldsymbol{M}_{\mathrm{T}}\boldsymbol{a}_r + \boldsymbol{B}_{\mathrm{T}}\boldsymbol{v}_r + \mathrm{sat}_3(\boldsymbol{F}_{\mathrm{T}}, \boldsymbol{K}_{\mathrm{T}}(\boldsymbol{p}_r \ominus \boldsymbol{p}_{x,\mathrm{prv}})). \tag{26}$$

The expression (23) can be seen as an algebraic problem with respect to the task-space acceleration $\boldsymbol{a}_x \in \mathbb{R}^6$, but to incorporate it into the framework of Fig. 4, it should be reformulated as a problem with respect to the joint-space acceleration $\boldsymbol{\alpha}_x \in \mathbb{R}^n$. Moreover, because the robot is assumed to have torque sensors, we need to replace $\boldsymbol{f}_s$ by $\boldsymbol{\tau}_s$ through the relation (21). Note that $\boldsymbol{a}_x$ and $\boldsymbol{\alpha}_x$ are related by

$$\boldsymbol{a}_x = \boldsymbol{J}(\boldsymbol{q}_{x,\mathrm{prv}})\boldsymbol{\alpha}_x + \boldsymbol{H}(\boldsymbol{q}_{x,\mathrm{prv}}, \boldsymbol{u}_{x,\mathrm{prv}})(\boldsymbol{u}_{x,\mathrm{prv}} + T\boldsymbol{\alpha}_x) \tag{27}$$

where $\boldsymbol{H}(\boldsymbol{q}, \boldsymbol{u})$ is the Jacobian rate-of-change, i.e., $\boldsymbol{H}(\boldsymbol{q}, \dot{\boldsymbol{q}}) \triangleq d\boldsymbol{J}(\boldsymbol{q})/dt$, which can be computed by conventional methods, such as [28, Sec. 5.5] and [29]. Therefore, by substituting (27) into (23) and left-multiplying its both sides by $\boldsymbol{J}(\boldsymbol{q}_s)^T$, one can obtain the following:

$$\begin{aligned}&\boldsymbol{J}(\boldsymbol{q}_s)^T\hat{\boldsymbol{C}}_{\mathrm{T}}(\boldsymbol{J}(\boldsymbol{q}_{x,\mathrm{prv}}) + T\boldsymbol{H}(\boldsymbol{q}_{x,\mathrm{prv}}, \boldsymbol{u}_{x,\mathrm{prv}}))\boldsymbol{\alpha}_x\\ &\quad - \boldsymbol{J}(\boldsymbol{q}_s)^T\left(\hat{\boldsymbol{b}}_{\mathrm{T}} - \hat{\boldsymbol{C}}_{\mathrm{T}}\boldsymbol{H}(\boldsymbol{q}_{x,\mathrm{prv}}, \boldsymbol{u}_{x,\mathrm{prv}})\boldsymbol{u}_{x,\mathrm{prv}}\right) - \boldsymbol{\tau}_s = \boldsymbol{0}_n.\end{aligned} \tag{28}$$

The solution to this problem is $\boldsymbol{\alpha}_x$, which is consistent with the task-space proxy dynamics (20).

Meanwhile, the joint-space proxy dynamics is given in the following continuous-time representation:

$$\dot{\boldsymbol{q}}_x = \boldsymbol{u}_x,\ \dot{\boldsymbol{u}}_x = \boldsymbol{\alpha}_x \tag{29a}$$

$$\boldsymbol{M}(\boldsymbol{\alpha}_x - \boldsymbol{\alpha}_r) + \boldsymbol{B}(\boldsymbol{u}_x - \boldsymbol{u}_r) + \mathrm{sat}_1(\boldsymbol{F}, \boldsymbol{K}(\boldsymbol{q}_x - \boldsymbol{q}_r)) = \boldsymbol{\tau}_s \tag{29b}$$

where the matrices $\boldsymbol{M}$, $\boldsymbol{B}$, and $\boldsymbol{K} \in \mathbb{R}^{n\times n}$ are the inertia, viscosity, and stiffness matrices, respectively, for the joint-space proxy dynamics, and $\boldsymbol{u}_r \triangleq \dot{\boldsymbol{q}}_r$ and $\boldsymbol{\alpha}_r \triangleq \dot{\boldsymbol{u}}_r$. They are diagonal positive-definite matrices. In the third term of the left-hand side

of (29b), the function sat_1 is the one defined in (2), and $\boldsymbol{F} \in \mathbb{R}^n$ is the vector of the limits for the forces of the joint-space proxy springs. A discrete-time approximation of (29) can be given as follows:

$$\boldsymbol{q}_x = \boldsymbol{q}_{x,\mathrm{prv}} + T\boldsymbol{u}_x,\ \boldsymbol{u}_x = \boldsymbol{u}_{x,\mathrm{prv}} + T\boldsymbol{\alpha}_x \tag{30a}$$

$$\begin{aligned}&\boldsymbol{M}\left(\boldsymbol{\alpha}_x - \boldsymbol{\alpha}_r\right) + \boldsymbol{B}(\boldsymbol{u}_{x,\mathrm{prv}} + T\boldsymbol{\alpha}_x - \boldsymbol{u}_r)\\ &\quad + \mathrm{sat}_1(\boldsymbol{F}, \boldsymbol{K}(\boldsymbol{q}_{x,\mathrm{prv}} - \boldsymbol{q}_r)) = \boldsymbol{\tau}_s.\end{aligned} \tag{30b}$$

One can rewrite (30b) as follows:

$$\hat{\boldsymbol{C}}_{\mathrm{J}}\boldsymbol{\alpha}_x - \hat{\boldsymbol{b}}_{\mathrm{J}} - \boldsymbol{\tau}_s = \boldsymbol{0}_n \tag{31}$$

where

$$\hat{\boldsymbol{C}}_{\mathrm{J}} \triangleq \boldsymbol{M} + T\boldsymbol{B} \tag{32}$$

$$\hat{\boldsymbol{b}}_{\mathrm{J}} \triangleq -\boldsymbol{B}\boldsymbol{u}_{x,\mathrm{prv}} + \boldsymbol{\tau}_{re} \tag{33}$$

$$\boldsymbol{\tau}_{re} \triangleq \boldsymbol{M}\boldsymbol{\alpha}_r + \boldsymbol{B}\boldsymbol{u}_r + \mathrm{sat}_1(\boldsymbol{F}, \boldsymbol{K}(\boldsymbol{q}_r - \boldsymbol{q}_{x,\mathrm{prv}})). \tag{34}$$

The problem (31) can be seen as a problem with respect to $\boldsymbol{\alpha}_x$ that is consistent with the joint-space proxy dynamics (29).

The task-space proxy dynamics (28) and the joint-space proxy dynamics (31) are combined in the following manner:

$$\boldsymbol{\alpha}_x^* = \underset{\boldsymbol{\alpha}_x \in \mathbb{R}^6}{\mathrm{arglexmin}} \left\{ \|(28)\text{'s lhs}\|_{\boldsymbol{M}^{-1}}, \|(31)\text{'s lhs}\|_{\boldsymbol{M}^{-1}} \right\} \tag{35}$$

where "lhs" stands for the left-hand side. The expression (35) means that the task-space proxy dynamics (28) is prioritized over the joint-space proxy dynamics (31), and that the joint-space proxy dynamics is used only in the nullspace. The use of the weight matrix $\boldsymbol{M}^{-1}$ in (35) is for the asymptotic stability of the combined dynamics, which will be discussed in Section V. By using Corollary 1, an algorithm to solve the problem (35) can be given as follows:

$$\text{Function TwoProxies}(\boldsymbol{p}_{x,\mathrm{prv}}, \boldsymbol{v}_{x,\mathrm{prv}}, \boldsymbol{q}_{x,\mathrm{prv}}, \boldsymbol{u}_{x,\mathrm{prv}}, \boldsymbol{\tau}_s) \tag{36a}$$

$$\boldsymbol{J}_s := \boldsymbol{J}(\boldsymbol{q}_s) \tag{36b}$$

$$\boldsymbol{H}_{x,\mathrm{prv}} := \boldsymbol{H}(\boldsymbol{q}_{x,\mathrm{prv}}, \boldsymbol{u}_{x,\mathrm{prv}}) \tag{36c}$$

$$\hat{\boldsymbol{J}}_x := \boldsymbol{J}(\boldsymbol{q}_{x,\mathrm{prv}}) + T\boldsymbol{H}_{x,\mathrm{prv}} \tag{36d}$$

$$\boldsymbol{C}_{\mathrm{T}} := \boldsymbol{M}^{-h}\boldsymbol{J}_s^T(\boldsymbol{M}_{\mathrm{T}} + T\boldsymbol{B}_{\mathrm{T}})\hat{\boldsymbol{J}}_x \tag{36e}$$

$$\boldsymbol{C}_{\mathrm{J}} := \boldsymbol{M}^{-h}(\boldsymbol{M} + T\boldsymbol{B}) \tag{36f}$$

$$\boldsymbol{f}_{re} := \boldsymbol{M}_{\mathrm{T}}\boldsymbol{a}_r + \boldsymbol{B}_{\mathrm{T}}\boldsymbol{v}_r + \mathrm{sat}_3(\boldsymbol{F}_{\mathrm{T}}, \boldsymbol{K}_{\mathrm{T}}(\boldsymbol{p}_r \ominus \boldsymbol{p}_{x,\mathrm{prv}})) \tag{36g}$$

$$\boldsymbol{\tau}_{re} := \boldsymbol{M}\boldsymbol{\alpha}_r + \boldsymbol{B}\boldsymbol{u}_r + \mathrm{sat}_1(\boldsymbol{F}, \boldsymbol{K}(\boldsymbol{q}_r - \boldsymbol{q}_{x,\mathrm{prv}})) \tag{36h}$$

$$\begin{aligned}\boldsymbol{b}_{\mathrm{T}} := \boldsymbol{M}^{-h}\big(&\boldsymbol{J}_s^T\left(-\boldsymbol{B}_{\mathrm{T}}\boldsymbol{v}_{x,\mathrm{prv}}\right.\\ &\left.-(\boldsymbol{M}_{\mathrm{T}} + T\boldsymbol{B}_{\mathrm{T}})\boldsymbol{H}_{x,\mathrm{prv}}\boldsymbol{u}_{x,\mathrm{prv}} + \boldsymbol{f}_r + \boldsymbol{f}_{re}\right) + \boldsymbol{\tau}_s\big)\end{aligned} \tag{36i}$$

$$\boldsymbol{b}_{\mathrm{J}} := \boldsymbol{M}^{-h}(-\boldsymbol{B}\boldsymbol{u}_{x,\mathrm{prv}} + \boldsymbol{\tau}_{re} + \boldsymbol{\tau}_s) \tag{36j}$$

$$\boldsymbol{C}_{\mathrm{TJ}} := \boldsymbol{C}_{\mathrm{T}}\boldsymbol{C}_{\mathrm{J}}^{-1} \tag{36k}$$

$$\boldsymbol{\alpha}_x^* := \boldsymbol{C}_{\mathrm{J}}^{-1}\boldsymbol{C}_{\mathrm{TJ}}^{+}\boldsymbol{b}_{\mathrm{T}} + \boldsymbol{C}_{\mathrm{J}}^{-1}\left(\boldsymbol{I}_n - \boldsymbol{C}_{\mathrm{TJ}}^{+}\boldsymbol{C}_{\mathrm{TJ}}\right)\boldsymbol{b}_{\mathrm{J}} \tag{36l}$$

$$\boldsymbol{u}_x^* := \boldsymbol{u}_{x,\mathrm{prv}} + T\boldsymbol{\alpha}_x^* \tag{36m}$$

$$\boldsymbol{q}_x^* := \boldsymbol{q}_{x,\mathrm{prv}} + T\boldsymbol{u}_x^* \tag{36n}$$

$$\text{Return } \boldsymbol{q}_x^*. \tag{36o}$$

It should be noted that the solution of (35) is $\boldsymbol{\alpha}_x^*$ obtained by (36l) and that the output of this function is its resultant proxy position $\boldsymbol{q}_x^*$. This function is to be used in the first line of the proposed controller algorithm (18). Recall that $\boldsymbol{M}^{-h}$ is a matrix satisfying $\boldsymbol{M}^{-1} = \boldsymbol{M}^{-hT}\boldsymbol{M}^{-h}$, as defined in Section II-A. Specifically, if $\boldsymbol{M}$ is a diagonal positive-definite matrix, $\boldsymbol{M}^{-h}$ can be simply chosen as $\boldsymbol{M}^{-h} = \boldsymbol{M}^{-1/2}$, which is the diagonal matrix whose diagonal elements are the reciprocals of the square roots of the diagonal elements of $\boldsymbol{M}$.

C. Computation of the Pseudoinverse $\boldsymbol{C}_{\mathrm{TJ}}^{+}$

We now discuss the computation of the pseudoinverse $\boldsymbol{C}_{\mathrm{TJ}}^{+}$ in the function TwoProxies, i.e., the algorithm (36). The matrix $\boldsymbol{C}_{\mathrm{TJ}}$ is an $n \times n$ square matrix, but it is not invertible because its rank is at most 6 and can be less in the singular configurations. The matrix $\boldsymbol{C}_{\mathrm{TJ}}$ can be decomposed as $\boldsymbol{C}_{\mathrm{TJ}} = \boldsymbol{C}_s\boldsymbol{C}_x$ where

$$\boldsymbol{C}_s \triangleq \boldsymbol{M}^{-h}\boldsymbol{J}_s^T(\boldsymbol{M}_{\mathrm{T}} + T\boldsymbol{B}_{\mathrm{T}}) \in \mathbb{R}^{n\times 6} \tag{37}$$

$$\boldsymbol{C}_x \triangleq \hat{\boldsymbol{J}}_x(\boldsymbol{M} + T\boldsymbol{B})^{-1}\boldsymbol{M}^h \in \mathbb{R}^{6\times n}. \tag{38}$$

Therefore, if both $\boldsymbol{C}_s$ and $\boldsymbol{C}_x$ are full-rank, we have $\boldsymbol{C}_{\mathrm{TJ}}^{+} = \boldsymbol{C}_x^{+}\boldsymbol{C}_s^{+}$. Thus, $\boldsymbol{C}_{\mathrm{TJ}}^{+}$ can be approximately obtained as follows:

$$\boldsymbol{C}_{\mathrm{TJ}}^{+} \approx \boldsymbol{C}_x^T(\boldsymbol{C}_x\boldsymbol{C}_x^T + \varepsilon_x\boldsymbol{I}_6)^{-1}(\boldsymbol{C}_s^T\boldsymbol{C}_s + \varepsilon_s\boldsymbol{I}_6)^{-1}\boldsymbol{C}_s^T \tag{39}$$

where ε_x and ε_s are small positive values to deal with the case where $\boldsymbol{J}_x$, $\boldsymbol{J}_s$, or both are rank-deficient. This approximation can be seen as an application of the damped pseudoinverses (cf., e.g., [15], [30], [31]). It requires careful choice of the values of ε_x and ε_s, and can cause a certain level of inaccuracy even when the robot is away from singular configurations.

The following introduces an alternative approximation of $\boldsymbol{C}_{\mathrm{TJ}}^{+}$ that coincides with the exact $\boldsymbol{C}_{\mathrm{TJ}}^{+}$ when the robot is outside a specified distance from singular configurations. Recall that the matrix $\boldsymbol{C}_{\mathrm{TJ}} \in \mathbb{R}^{n\times n}$ can be decomposed as $\boldsymbol{C}_{\mathrm{TJ}} = \boldsymbol{U}\boldsymbol{\Sigma}\boldsymbol{V}^T$ where $\boldsymbol{U} \in \mathbb{R}^{n\times n}$ and $\boldsymbol{V} \in \mathbb{R}^{n\times n}$ are orthogonal matrices and $\boldsymbol{\Sigma} \in \mathbb{R}^{n\times n}$ is a diagonal matrix whose diagonal elements are the singular values of the matrix $\boldsymbol{C}_{\mathrm{TJ}}$. The pseudoinverse $\boldsymbol{C}_{\mathrm{TJ}}^{+} \in \mathbb{R}^{n\times n}$ is obtained as $\boldsymbol{C}_{\mathrm{TJ}}^{+} = \boldsymbol{V}\boldsymbol{\Sigma}^{+}\boldsymbol{U}^T$. Here, the matrix $\boldsymbol{\Sigma}^{+}$ is the $n \times n$ diagonal matrix whose ith diagonal element is

$$\sigma_i^{+} \triangleq \begin{cases} 1/\sigma_i & \text{if } \sigma_i \neq 0 \\ 0 & \text{if } \sigma_i = 0 \end{cases} \tag{40}$$

where σ_i is the ith diagonal element of $\boldsymbol{\Sigma}$. This definition injects the discontinuity around $\sigma_i = 0$, and also causes an excessively large value of σ_i^{+} when σ_i is nonzero but very small. One alternative is to replace σ_i^{+} by the following:

$$\sigma_i^{\oplus} \triangleq \frac{\sigma_i}{\max(\sigma_i^2, \varepsilon^2)} = \begin{cases} 1/\sigma_i & \text{if } |\sigma_i| > \varepsilon \\ \sigma_i/\varepsilon^2 & \text{if } |\sigma_i| \leq \varepsilon \end{cases} \tag{41}$$

where $\varepsilon > 0$ is a parameter appropriately chosen. With this replacement, one can obtain the matrix $\boldsymbol{C}_{\mathrm{TJ}}^{\oplus} \triangleq \boldsymbol{U}\boldsymbol{\Sigma}^{\oplus}\boldsymbol{V}^T$ where $\boldsymbol{\Sigma}^{\oplus}$ is the $n \times n$ diagonal matrix with the diagonal elements defined in (41). Hereafter, we refer to $\boldsymbol{C}_{\mathrm{TJ}}^{\oplus}$ as a *continualized pseudoinverse* of $\boldsymbol{C}_{\mathrm{TJ}}$.

IEEE Transactions on Robotics (T-RO) paper, presented at ICRA 2026, Vienna, Austria. Cite as T-RO paper.

One advantage of the presented continualized pseudoinverse $\boldsymbol{C}_{\mathrm{TJ}}^{\oplus}$ is that it exactly coincides with the original pseudoinverse $\boldsymbol{C}_{\mathrm{TJ}}^{+}$ as long as the singular values are either the exact zero or above the threshold ε. As for $\boldsymbol{C}_{\mathrm{TJ}}$, it has six nonzero singular values when $\boldsymbol{J}_x$ and $\boldsymbol{J}_s$ are full-rank, i.e., when the robot is not in the singular configurations. Therefore, as long as its largest six singular values are above the threshold ε, $\boldsymbol{C}_{\mathrm{TJ}}^{\oplus} = \boldsymbol{C}_{\mathrm{TJ}}^{+}$ is satisfied, and thus $\boldsymbol{\alpha}_x^*$ obtained by (36l) is the accurate solution of the lexicographic minimization problem (35).

It should be noted that all elements of $\boldsymbol{C}_{\mathrm{TJ}}$ are dimensionless quantities, and consequently, the singular values of $\boldsymbol{C}_{\mathrm{TJ}}$ are also dimensionless. This property is not generally true for arbitrary matrices; a matrix whose elements have different physical dimensions may have singular values having no consistent physical dimensions. Because the singular values of $\boldsymbol{C}_{\mathrm{TJ}}$ are dimensionless and physically consistent, the threshold ε used in (41) can also be understood as a physically consistent dimensionless quantity. This is not the case with (39), where neither ε_s nor ε_x has a consistent physical dimension.

Although the threshold ε is physically consistent, its choice still requires careful consideration. The threshold ε determines whether the task-space or the joint-space admittance is active in each direction; the task-space admittance is active in directions in which the singular value of $\boldsymbol{C}_{\mathrm{TJ}}$ is above ε, and the joint-space admittance is active otherwise. If T is small enough, the matrix $\boldsymbol{C}_{\mathrm{TJ}}$ reduces to the following:

$$\boldsymbol{C}_{\mathrm{TJ}} \approx \boldsymbol{M}^{-h}\boldsymbol{J}_s^T\boldsymbol{M}_{\mathrm{T}}\boldsymbol{J}_x\boldsymbol{M}^{-hT}. \tag{42}$$

The matrix $\boldsymbol{J}_s^T\boldsymbol{M}_{\mathrm{T}}\boldsymbol{J}_x \in \mathbb{R}^{n\times n}$ appearing here can be interpreted as *the task-space inertia evaluated in the joint space.* Thus, $\boldsymbol{C}_{\mathrm{TJ}}$ can be interpreted to represent the ratios of the task-space inertia $\boldsymbol{J}_s^T\boldsymbol{M}_{\mathrm{T}}\boldsymbol{J}_x$ to the joint-space inertia $\boldsymbol{M}$ evaluated in the joint space. In fact, in the vicinity of the singular configuration, the task-space inertia $\boldsymbol{J}_s^T\boldsymbol{M}_{\mathrm{T}}\boldsymbol{J}_x$ becomes lower in a particular direction in the joint space, which jeopardizes the stability. In this light, ε could be chosen considering the lowest permissible task-space inertia in comparison to the joint-space inertia. Although we currently do not have a definitive guideline for the choice of ε, we chose $\varepsilon = 0.03$ in our experimental setup comprising a seven-DOF manipulator, detailed in Section VI, through some preliminary experiments.

D. Parameter Tuning

The proposed controller depends on several parameters that need to be chosen appropriately. Although clear tuning guidelines remain an open problem, factors relevant to the choice of parameters are summarized as follows.

1) The torque limit F_c for each joint, which is a parameter of the function SatPosCtrl, should be set considering the rated torque of the joint actuator or safety requirements for the application. It may need to be chosen considering the tradeoff between the control performance (such as load-carrying capacity) and the safety.
2) The PID gains $\{K_c, L_c, B_c\}$ for each joint, which are also parameters of the function SatPosCtrl, should be chosen so that the joint-level PID position control performs as accurately as possible. These gains can be tuned through trial and error or using conventional methods, such as Ziegler–Nichols ultimate sensitivity method [32].
3) The joint-space proxy parameters $\{\boldsymbol{M}, \boldsymbol{B}, \boldsymbol{K}, \boldsymbol{F}\}$ should be chosen to realize stable joint-independent admittance control. In general, lower $\boldsymbol{M}$ and $\boldsymbol{B}$ increase responsiveness but may deteriorate the stability. This tuning can be performed by temporarily disabling the task-space admittance control by overwriting $\boldsymbol{C}_{\mathrm{TJ}}^{+} := \boldsymbol{O}_{7\times 7}$ in the function TwoProxies, which makes the controller equivalent to the collection of 1-D TBAC [10] independently applied to the joints.
4) The task-space proxy parameters $\{\boldsymbol{M}_{\mathrm{T}}, \boldsymbol{B}_{\mathrm{T}}, \boldsymbol{K}_{\mathrm{T}}, \boldsymbol{F}_{\mathrm{T}}\}$ should be chosen to realize stable task-space admittance control. The tuning of these parameters can be performed in the same principle as those for the joint-space parameters, in the sense that lower inertia and viscosity lead to higher responsiveness but lower stability.
5) The parameter ε should be chosen as small as possible without causing oscillations when the robot is fully stretched. Based on experimental observations, $\varepsilon = 0.03$ was found to be a reasonable choice for our experimental setup comprising the seven-DOF manipulator introduced in Section VI.

V. Stability Analysis

A. Combined Proxy Dynamics

We here analyze the stability properties of the combined proxy dynamics, which are defined in Section IV-B and realized by the algorithm (36) in the discrete-time domain. For simplicity, we assume that the position controller is not saturated and is perfectly accurate. Then, we have $\boldsymbol{J}_x = \boldsymbol{J}_s$. For notational brevity, we omit the subscript x within this section. Then, the continuous-time representation of the combined proxy dynamics realized by the algorithm (36) can be written as follows:

$$\dot{\boldsymbol{q}} = \boldsymbol{u} \tag{43a}$$

$$\begin{aligned}\dot{\boldsymbol{u}} = \underset{\boldsymbol{\alpha}\in\mathbb{R}^n}{\mathrm{arglexmin}} \big(\{ &\|\boldsymbol{J}^T\boldsymbol{M}_{\mathrm{T}}\boldsymbol{J}\boldsymbol{\alpha} + \boldsymbol{J}^T(\boldsymbol{B}_{\mathrm{T}}\boldsymbol{J} + \boldsymbol{M}_{\mathrm{T}}\boldsymbol{H})\boldsymbol{u} \\ &+ \boldsymbol{J}^T\boldsymbol{\theta}_{\mathrm{T}}(\boldsymbol{\Phi}(\boldsymbol{q}) \ominus \boldsymbol{p}_r) - \boldsymbol{J}^T\boldsymbol{f}_e\|_{\boldsymbol{M}^{-1}}^2 \\ &\|\boldsymbol{M}\boldsymbol{\alpha} + \boldsymbol{B}\boldsymbol{u} + \boldsymbol{\theta}(\boldsymbol{q} - \boldsymbol{q}_r) - \boldsymbol{\tau}_e\|_{\boldsymbol{M}^{-1}}^2\}\big)\end{aligned} \tag{43b}$$

where

$$\boldsymbol{f}_e \triangleq \boldsymbol{M}_{\mathrm{T}}\boldsymbol{a}_r + \boldsymbol{B}_{\mathrm{T}}\boldsymbol{v}_r + \boldsymbol{f}_{sr} \tag{44}$$

$$\boldsymbol{\tau}_e \triangleq \boldsymbol{M}\boldsymbol{\alpha}_r + \boldsymbol{B}\boldsymbol{u}_r + \boldsymbol{\tau}_s \tag{45}$$

$$\boldsymbol{f}_{sr} \triangleq \boldsymbol{f}_s + \boldsymbol{f}_r \tag{46}$$

and $\boldsymbol{\theta}_{\mathrm{T}} : \mathbb{R}^6 \to \mathbb{R}^6$ and $\boldsymbol{\theta} : \mathbb{R}^n \to \mathbb{R}^n$ are functions defined as follows:

$$\boldsymbol{\theta}_{\mathrm{T}}(\Delta\boldsymbol{p}) \triangleq \mathrm{sat}_3(\boldsymbol{F}_{\mathrm{T}}, \boldsymbol{K}_{\mathrm{T}}\Delta\boldsymbol{p}) \tag{47}$$

$$\boldsymbol{\theta}(\Delta\boldsymbol{q}) \triangleq \mathrm{sat}_1(\boldsymbol{F}, \boldsymbol{K}\Delta\boldsymbol{q}). \tag{48}$$

Note that the state vector of the system is $[\boldsymbol{q}^T, \boldsymbol{u}^T]^T \in \mathbb{R}^{2n}$.

With some tedious but straightforward derivations using Corollary 1, one can rewrite (43b) in the following form:

$$\begin{aligned}\dot{\boldsymbol{u}} = & -\boldsymbol{J}^{\#}\boldsymbol{M}_{\mathrm{T}}^{-1}\left((\boldsymbol{B}_{\mathrm{T}}\boldsymbol{J}+\boldsymbol{M}_{\mathrm{T}}\boldsymbol{H})\boldsymbol{u}+\boldsymbol{\theta}_{\mathrm{T}}(\boldsymbol{\Phi}(\boldsymbol{q})\ominus\boldsymbol{p}_r)-\boldsymbol{f}_e\right)\\ & -\boldsymbol{M}^{-1}(\boldsymbol{I}_n-\boldsymbol{J}^T\boldsymbol{J}^{\#T})(\boldsymbol{B}\boldsymbol{u}+\boldsymbol{\theta}(\boldsymbol{q}-\boldsymbol{q}_r)-\boldsymbol{\tau}_e) \quad (49)\end{aligned}$$

where

$$\boldsymbol{J}^{\#}\triangleq\boldsymbol{M}^{-hT}(\boldsymbol{M}_{\mathrm{T}}^{hT}\boldsymbol{J}\boldsymbol{M}^{-hT})^{+}\boldsymbol{M}_{\mathrm{T}}^{hT}\in\mathbb{R}^{n\times 6}. \quad (50)$$

Recall that $\boldsymbol{M}_{\mathrm{T}}=\boldsymbol{M}_{\mathrm{T}}^{h}\boldsymbol{M}_{\mathrm{T}}^{hT}$ and $\boldsymbol{M}^{-1}=\boldsymbol{M}^{-hT}\boldsymbol{M}^{-h}$. The matrix $\boldsymbol{J}^{\#}$ satisfies the following relations:

$$\boldsymbol{J}^{\#}\boldsymbol{J}\boldsymbol{J}^{\#}=\boldsymbol{J}^{\#} \quad (51a)$$

$$\boldsymbol{J}\boldsymbol{J}^{\#}\boldsymbol{J}=\boldsymbol{J} \quad (51b)$$

$$\boldsymbol{J}\boldsymbol{J}^{\#}\boldsymbol{M}_{\mathrm{T}}^{-1}=\boldsymbol{M}_{\mathrm{T}}^{-1}\boldsymbol{J}^{\#T}\boldsymbol{J}^{T}=\boldsymbol{J}\boldsymbol{J}^{\#}\boldsymbol{M}_{\mathrm{T}}^{-1}\boldsymbol{J}^{\#T}\boldsymbol{J}^{T} \quad (51c)$$

$$\boldsymbol{J}^{\#}\boldsymbol{J}\boldsymbol{M}^{-1}=\boldsymbol{M}^{-1}\boldsymbol{J}^{T}\boldsymbol{J}^{\#T}=\boldsymbol{J}^{\#}\boldsymbol{J}\boldsymbol{M}^{-1}\boldsymbol{J}^{T}\boldsymbol{J}^{\#T}. \quad (51d)$$

Note that $\boldsymbol{J}^{\#}$ has similar properties to those of the dynamically consistent Jacobian inverse [33], [34].

Left-multiplying the both sides of (49) by $\boldsymbol{J}$ yields the following:

$$\begin{aligned}\boldsymbol{J}\dot{\boldsymbol{u}} = & -\boldsymbol{M}_{\mathrm{T}}^{-1}\boldsymbol{J}^{\#T}\boldsymbol{J}^{T}\left((\boldsymbol{B}_{\mathrm{T}}\boldsymbol{J}+\boldsymbol{M}_{\mathrm{T}}\boldsymbol{H})\boldsymbol{u}\right.\\ & \left.+\boldsymbol{\theta}_{\mathrm{T}}(\boldsymbol{\Phi}(\boldsymbol{q})\ominus\boldsymbol{p}_r)-\boldsymbol{f}_e\right). \quad (52)\end{aligned}$$

In addition, left-multiplying the both sides of (52) by $\boldsymbol{J}^T\boldsymbol{M}_{\mathrm{T}}$ yields the following:

$$\boldsymbol{J}^T\boldsymbol{M}_{\mathrm{T}}\frac{d\boldsymbol{J}\boldsymbol{u}}{dt}=-\boldsymbol{J}^T\left(\boldsymbol{B}_{\mathrm{T}}\boldsymbol{J}\boldsymbol{u}+\boldsymbol{\theta}_{\mathrm{T}}(\boldsymbol{\Phi}(\boldsymbol{q})\ominus\boldsymbol{p}_r)-\boldsymbol{f}_e\right) \quad (53)$$

where we used $d\boldsymbol{J}\boldsymbol{u}/dt=\dot{\boldsymbol{v}}=\boldsymbol{H}\boldsymbol{u}+\boldsymbol{J}\dot{\boldsymbol{u}}$. Equation (53) can be seen as a representation of the task-space dynamics realized by (49).

Moreover, left-multiplying (52) by $\boldsymbol{J}^{\#}$ results in

$$\begin{aligned}\boldsymbol{J}^{\#}\boldsymbol{J}\dot{\boldsymbol{u}} = & -\boldsymbol{J}^{\#}\boldsymbol{M}_{\mathrm{T}}^{-1}\left((\boldsymbol{B}_{\mathrm{T}}\boldsymbol{J}+\boldsymbol{M}_{\mathrm{T}}\boldsymbol{H})\boldsymbol{u}\right.\\ & \left.+\boldsymbol{\theta}_{\mathrm{T}}(\boldsymbol{\Phi}(\boldsymbol{q})\ominus\boldsymbol{p}_r)-\boldsymbol{f}_e\right) \quad (54)\end{aligned}$$

where we used $\boldsymbol{J}^{\#}\boldsymbol{M}_{\mathrm{T}}^{-1}\boldsymbol{J}^{\#T}\boldsymbol{J}^{T}=\boldsymbol{J}^{\#}\boldsymbol{M}_{\mathrm{T}}^{-1}$. Noticing that the right-hand side of (54) is identical to the first term of the right-hand side of (49), one can rewrite (49) as follows:

$$\begin{aligned}\dot{\boldsymbol{u}} = & -\boldsymbol{M}^{-1}(\boldsymbol{I}_n-\boldsymbol{J}^T\boldsymbol{J}^{\#T})(\boldsymbol{B}\boldsymbol{u}+\boldsymbol{\theta}(\boldsymbol{q}-\boldsymbol{q}_r)-\boldsymbol{\tau}_e)\\ & +\boldsymbol{J}^{\#}\left(\dot{\boldsymbol{v}}-\boldsymbol{H}\boldsymbol{u}\right) \quad (55)\end{aligned}$$

where we used $\boldsymbol{J}\dot{\boldsymbol{u}}=\dot{\boldsymbol{v}}-\boldsymbol{H}\boldsymbol{u}$. Equation (55) can be seen as a representation of the joint-space dynamics realized by (49). The relations (53) and (55) will be used in the subsequent analysis.

B. Stability Under Constant References and Constant External Forces

This section restricts the discussion to the case where $\boldsymbol{p}_r$, $\boldsymbol{q}_r$, $\boldsymbol{f}_{sr}(=\boldsymbol{f}_s+\boldsymbol{f}_r)$, and $\boldsymbol{\tau}_s$ are constant, i.e., where $\boldsymbol{v}_r$, $\boldsymbol{a}_r$, $\boldsymbol{u}_r$, and $\boldsymbol{\alpha}_r$ are zero. Equilibria of the system under this restriction can be inferred by careful observation of (53) and (55), which are derived from (49); with (53) and (55), $\dot{\boldsymbol{u}}=\boldsymbol{0}_n$ and $\boldsymbol{u}=\boldsymbol{0}_n$ can hold true if $\boldsymbol{q}$ satisfies the following conditions:

$$\boldsymbol{J}^T(\boldsymbol{\theta}_{\mathrm{T}}(\boldsymbol{\Phi}(\boldsymbol{q})\ominus\boldsymbol{p}_r)-\boldsymbol{f}_{sr})=\boldsymbol{0}_n \quad (56)$$

$$(\boldsymbol{I}_n-\boldsymbol{J}^T\boldsymbol{J}^{\#T})(\boldsymbol{\theta}(\boldsymbol{q}-\boldsymbol{q}_r)-\boldsymbol{\tau}_s)=\boldsymbol{0}_n. \quad (57)$$

This means that the system is in equilibrium when $\boldsymbol{q}$ satisfies (56) $\wedge$ (57) and $\boldsymbol{u}=\boldsymbol{0}_n$. The following analysis investigates the stability of this equilibrium.

We here use the following functions:

$$\begin{aligned}V_{\mathrm{T}}\triangleq & \,\boldsymbol{u}^T\boldsymbol{J}^T\boldsymbol{M}_{\mathrm{T}}\boldsymbol{J}\boldsymbol{u}/2+\Theta_{\mathrm{T}}(\boldsymbol{\Phi}(\boldsymbol{q})\ominus\boldsymbol{p}_r)\\ & -\boldsymbol{f}_{sr}^T(\boldsymbol{\Phi}(\boldsymbol{q})\ominus\boldsymbol{p}_r) \quad (58)\end{aligned}$$

$$V_{\mathrm{J}}\triangleq\boldsymbol{u}^T\boldsymbol{M}\boldsymbol{u}/2+\Theta(\boldsymbol{q}-\boldsymbol{q}_r)-\boldsymbol{\tau}_s^T(\boldsymbol{q}-\boldsymbol{q}_r) \quad (59)$$

where $\Theta_{\mathrm{T}}:\mathbb{R}^6\to\mathbb{R}$ and $\Theta:\mathbb{R}^n\times\mathbb{R}^n\to\mathbb{R}$ are functions satisfying the following:

$$\frac{\partial\Theta_{\mathrm{T}}(\Delta\boldsymbol{p})}{\partial\Delta\boldsymbol{p}^T}=\boldsymbol{\theta}_{\mathrm{T}}(\Delta\boldsymbol{p}),\quad\frac{\partial\Theta(\Delta\boldsymbol{q})}{\partial\Delta\boldsymbol{q}^T}=\boldsymbol{\theta}(\Delta\boldsymbol{q}). \quad (60)$$

The functions V_{T} and V_{J} can be said to be the task- and joint-space energy functions, respectively, and the functions $\boldsymbol{\Theta}_{\mathrm{T}}$ and $\boldsymbol{\Theta}$ can be said to be the task- and joint-space elastic potential energy functions, respectively.

From (53), the task-space energy function V_{T} can be differentiated as follows:

$$\begin{aligned}\dot{V}_{\mathrm{T}} = & -\boldsymbol{u}^T\boldsymbol{J}^T\left(\boldsymbol{B}_{\mathrm{T}}\boldsymbol{J}\boldsymbol{u}+\boldsymbol{\theta}_{\mathrm{T}}(\boldsymbol{\Phi}(\boldsymbol{q})\ominus\boldsymbol{p}_r)-\boldsymbol{f}_{sr}\right)\\ & +(\boldsymbol{J}\boldsymbol{u})^T\boldsymbol{\theta}_{\mathrm{T}}(\boldsymbol{\Phi}(\boldsymbol{q})\ominus\boldsymbol{p}_r)-\boldsymbol{f}_{sr}^T\boldsymbol{J}\boldsymbol{u}\\ = & -\boldsymbol{u}^T\boldsymbol{J}^T\boldsymbol{B}_{\mathrm{T}}\boldsymbol{J}\boldsymbol{u}\le 0. \quad (61)\end{aligned}$$

The condition $\dot{V}_{\mathrm{T}}=0$ holds when $\boldsymbol{J}\boldsymbol{u}=\boldsymbol{0}_6$. From (53), the invariant set under the condition $\boldsymbol{J}\boldsymbol{u}=\boldsymbol{0}_6$ can be obtained as

$$\boldsymbol{\mathcal{X}}_{\mathrm{T}}\triangleq\{[\boldsymbol{q}^T,\boldsymbol{u}^T]^T\in\mathbb{R}^{2n}\mid\boldsymbol{J}\boldsymbol{u}=\boldsymbol{0}_6\wedge(56)\}. \quad (62)$$

Therefore, from LaSalle's invariance principle, the set $\boldsymbol{\mathcal{X}}_{\mathrm{T}}$ is positively invariant and asymptotically stable. That is, we have $\boldsymbol{v}\triangleq\boldsymbol{J}\boldsymbol{u}\to\boldsymbol{0}_6$ and $\boldsymbol{J}^T(\boldsymbol{\theta}_{\mathrm{T}}(\boldsymbol{\Phi}(\boldsymbol{q})\ominus\boldsymbol{p}_r)-\boldsymbol{f}_{sr})\to\boldsymbol{0}_n$ as $t\to\infty$.

Meanwhile, from (55), the joint-space energy function V_{J} can be differentiated as follows:

$$\begin{aligned}\dot{V}_{\mathrm{J}} = & \,\boldsymbol{u}^T(\boldsymbol{M}\dot{\boldsymbol{u}}+\boldsymbol{\theta}(\boldsymbol{q}-\boldsymbol{q}_r)-\boldsymbol{\tau}_s)\\ = & -\boldsymbol{u}^T(\boldsymbol{I}_n-\boldsymbol{J}^T\boldsymbol{J}^{\#T})\boldsymbol{B}\boldsymbol{u}+\boldsymbol{u}^T\boldsymbol{J}^T\boldsymbol{J}^{\#T}(\boldsymbol{\theta}(\boldsymbol{q}-\boldsymbol{q}_r)-\boldsymbol{\tau}_s)\\ & +\boldsymbol{u}^T\boldsymbol{M}\boldsymbol{J}^{\#}(\dot{\boldsymbol{v}}-\boldsymbol{H}\boldsymbol{u})\\ = & -\boldsymbol{u}^T\boldsymbol{B}\boldsymbol{u}+\boldsymbol{v}^T\boldsymbol{J}^{\#T}\left(\boldsymbol{B}\boldsymbol{u}+\boldsymbol{\theta}(\boldsymbol{q}-\boldsymbol{q}_r)-\boldsymbol{\tau}_s\right.\\ & \left.+\boldsymbol{M}\boldsymbol{J}^{\#}(\dot{\boldsymbol{v}}-\boldsymbol{H}\boldsymbol{u})\right). \quad (63)\end{aligned}$$

This expression implies that $\dot{V}_{\mathrm{J}}\le 0$ is satisfied when $\boldsymbol{v}=\boldsymbol{0}_6$, and that $\dot{V}_{\mathrm{J}}=0$ is satisfied when $\boldsymbol{u}=\boldsymbol{0}_n$. In addition, (55) implies that the invariant set under the condition (56) $\wedge\,\boldsymbol{u}=\boldsymbol{0}_n$ can be written as

$$\boldsymbol{\mathcal{X}}_{\mathrm{J}}\triangleq\{[\boldsymbol{q}^T,\boldsymbol{u}^T]^T\in\mathbb{R}^{2n}\mid\boldsymbol{u}=\boldsymbol{0}_n\wedge(56)\wedge(57)\}. \quad (64)$$

IEEE Transactions on Robotics (T-RO) paper, presented at ICRA 2026, Vienna, Austria. Cite as T-RO paper.

Therefore, from LaSalle's invariance principle, as long as $[\boldsymbol{q}^T, \boldsymbol{u}^T]^T \in \boldsymbol{\mathcal{X}}_{\mathrm{T}}$, the set $\boldsymbol{\mathcal{X}}_{\mathrm{J}} \subset \boldsymbol{\mathcal{X}}_{\mathrm{T}}$ is asymptotically stable. Because $\boldsymbol{\mathcal{X}}_{\mathrm{T}}$ is asymptotically reached by $[\boldsymbol{q}^T, \boldsymbol{u}^T]^T$, one can see that the set $\boldsymbol{\mathcal{X}}_{\mathrm{J}} \subset \boldsymbol{\mathcal{X}}_{\mathrm{T}}$ is also asymptotically stable with the combined proxy dynamics (43). This means that the task-space position $\boldsymbol{p} = \boldsymbol{\Phi}(\boldsymbol{q})$ eventually converges to the position satisfying (56) and the nullspace motion also eventually settles, bringing the entire system into a steady state at the configurations $\boldsymbol{q}$ satisfying (56) $\wedge$ (57).

If $\boldsymbol{f}_{sr}$ and $\boldsymbol{\tau}_s$ are zeros and $\boldsymbol{p}_r$ is within the reachable workspace of the robot except for the singular configurations, i.e., so that there exists $\boldsymbol{q}$ such that $\boldsymbol{\Phi}(\boldsymbol{q}) = \boldsymbol{p}_r$ and $\mathrm{rank}\, \boldsymbol{J}(\boldsymbol{q}) = 6$, the condition (56) $\wedge$ (57) reduces to

$$\boldsymbol{\Phi}(\boldsymbol{q}) = \boldsymbol{p}_r \ \wedge \ (\boldsymbol{I}_n - \boldsymbol{J}^T\boldsymbol{J}^{\#T})\boldsymbol{\theta}(\boldsymbol{q} - \boldsymbol{q}_r) = \boldsymbol{0}_n. \tag{65}$$

Moreover, if $\boldsymbol{f}_{sr}$ and $\boldsymbol{\tau}_s$ are zeros and $\boldsymbol{q}_r$ and $\boldsymbol{p}_r$ are set as $\boldsymbol{p}_r = \boldsymbol{\Phi}(\boldsymbol{q}_r)$ and $\mathrm{rank}\, \boldsymbol{J}(\boldsymbol{q}_r) = 6$, the condition (56) $\wedge$ (57) reduces to $\boldsymbol{q} = \boldsymbol{q}_r$. This means that, if $\boldsymbol{f}_{sr}$ and $\boldsymbol{\tau}_s$ are zeros, $\boldsymbol{p}_r$ is set within the reachable workspace of the robot, and $\boldsymbol{q}_r$ is set consistent with $\boldsymbol{p}_r$, the combined proxy dynamics (43) drives $\boldsymbol{q}$ to $\boldsymbol{q}_r$, resulting in the task-space position satisfying $\boldsymbol{\Phi}(\boldsymbol{q}) = \boldsymbol{p}_r$.

Remark 1: It should be noted that, when $\boldsymbol{J}$ is full-rank, $\boldsymbol{J}^{\#}$ in (50) reduces to $\boldsymbol{J}^{\#} = \boldsymbol{M}^{-1}\boldsymbol{J}^T(\boldsymbol{J}\boldsymbol{M}^{-1}\boldsymbol{J}^T)^{-1}$, which coincides with the dynamically consistent Jacobian inverse [33], [34]. According to its original definition, the dynamically consistent Jacobian inverse $\boldsymbol{J}^{\#}$ is a matrix that satisfies the following:

$$\forall \boldsymbol{\tau} \in \mathbb{R}^n, \quad \boldsymbol{J}\boldsymbol{M}^{-1}\boldsymbol{\tau} = \boldsymbol{J}\boldsymbol{M}^{-1}\boldsymbol{J}^T\boldsymbol{J}^{\#T}\boldsymbol{\tau} \tag{66}$$

which means that $\boldsymbol{J}^{\#T}$ maps any torque vector $\boldsymbol{\tau}$ to a task-space force vector $\boldsymbol{f}$ that results in the same task-space acceleration $\boldsymbol{a}$ as $\boldsymbol{\tau}$ results in according to the joint-space dynamics. The matrix $\boldsymbol{J}^{\#}$ defined in (50) satisfies (66) and also the following:

$$\forall \boldsymbol{\tau} \in \mathbb{R}^n, \ \exists \boldsymbol{\alpha} \in \mathbb{R}^n \text{ s.t. } \boldsymbol{J}\boldsymbol{\alpha} = \boldsymbol{M}_{\mathrm{T}}^{-1}\boldsymbol{J}^{\#T}\boldsymbol{\tau} \tag{67}$$

which means that $\boldsymbol{J}^{\#T}$ maps any torque vector $\boldsymbol{\tau}$ to a task-space force vector $\boldsymbol{f}$ that results in a kinematically realizable task-space acceleration $\boldsymbol{a}$ according to the task-space dynamics. In conclusion, $\boldsymbol{J}^{\#}$ in (50) acts as a Jacobian inverse that is consistent both in the joint-space dynamics and the task-space dynamics.

Remark 2: The discrete-time algorithm (36) involves $\boldsymbol{C}_{\mathrm{TJ}}^{+}$ instead of $\boldsymbol{J}^{\#}$. Recall that, by setting T small enough, $\boldsymbol{C}_{\mathrm{TJ}}$ can be written as (42). From this, its pseudoinverse can be given as follows:

$$\begin{aligned}\boldsymbol{C}_{\mathrm{TJ}}^{+} &= (\boldsymbol{M}_{\mathrm{T}}^{hT}\boldsymbol{J}_x\boldsymbol{M}^{-hT})^{+}(\boldsymbol{M}^{-h}\boldsymbol{J}_s^T\boldsymbol{M}_{\mathrm{T}}^{h})^{+} \\ &= \boldsymbol{M}^{hT}\boldsymbol{J}_x^{\#}\boldsymbol{M}_{\mathrm{T}}^{-1}\boldsymbol{J}_s^{\#T}\boldsymbol{M}^{h}.\end{aligned} \tag{68}$$

This implies that the proposed algorithm (36) implicitly and approximately involves the matrices $\boldsymbol{J}_x^{\#}$ and $\boldsymbol{J}_s^{\#}$. In addition, the term $\boldsymbol{C}_{\mathrm{TJ}}^{+}\boldsymbol{C}_{\mathrm{TJ}}$, which appears in (36l), is related to $\boldsymbol{J}_x^{\#}$ and $\boldsymbol{J}_s^{\#}$ by the following:

$$\begin{aligned}\boldsymbol{C}_{\mathrm{TJ}}^{+}\boldsymbol{C}_{\mathrm{TJ}} &= \boldsymbol{M}^{hT}\boldsymbol{J}_x^{\#}\boldsymbol{M}_{\mathrm{T}}^{-1}\boldsymbol{J}_s^{\#T}\boldsymbol{J}_s^T\boldsymbol{M}_{\mathrm{T}}\boldsymbol{J}_x\boldsymbol{M}^{-hT} \\ &= \boldsymbol{M}^{hT}\boldsymbol{J}_x^{\#}\boldsymbol{J}_s\boldsymbol{J}_s^{\#}\boldsymbol{J}_x\boldsymbol{M}^{-hT}\end{aligned} \tag{69}$$

and, by assuming $\boldsymbol{J}_s \approx \boldsymbol{J}_x = \boldsymbol{J}$, it reduces to

$$\boldsymbol{C}_{\mathrm{TJ}}^{+}\boldsymbol{C}_{\mathrm{TJ}} \approx \boldsymbol{M}^{hT}\boldsymbol{J}^{\#}\boldsymbol{J}\boldsymbol{M}^{-hT} = \boldsymbol{M}^{-h}\boldsymbol{J}^T\boldsymbol{J}^{\#T}\boldsymbol{M}^{h}. \tag{70}$$

This expression allows for the interpretation of (36l) in relation to the so-called nullspace projector [20], [22], which may be helpful for further theoretical investigation.

C. Effect of the Weight Matrices

Here, we show that the weight matrix $\boldsymbol{M}^{-1}$ appearing in the discrete-time representation (35) and the continuous-time one (43b) is necessary to guarantee the stability of the task-space dynamics. Let us consider the case where (43b) is replaced by

$$\begin{aligned}\dot{\boldsymbol{u}} = \underset{\boldsymbol{\alpha}\in\mathbb{R}^n}{\mathrm{arglexmin}} \big(\{ &\|\boldsymbol{J}^T\boldsymbol{M}_{\mathrm{T}}\boldsymbol{J}\boldsymbol{\alpha} + \boldsymbol{J}^T(\boldsymbol{B}_{\mathrm{T}}\boldsymbol{J} + \boldsymbol{M}_{\mathrm{T}}\boldsymbol{H})\boldsymbol{u} \\ &+ \boldsymbol{J}^T\boldsymbol{\theta}_{\mathrm{T}}(\boldsymbol{\Phi}(\boldsymbol{q}) \ominus \boldsymbol{p}_r) - \boldsymbol{J}^T\boldsymbol{f}_e\|^2_{\boldsymbol{X}^T\boldsymbol{X}} \\ &\|\boldsymbol{M}\boldsymbol{\alpha} + \boldsymbol{B}\boldsymbol{u} + \boldsymbol{\theta}(\boldsymbol{q} - \boldsymbol{q}_r) - \boldsymbol{\tau}_e\|^2_{\boldsymbol{Y}^T\boldsymbol{Y}}\}\big)\end{aligned} \tag{71}$$

where $\boldsymbol{X}$ and $\boldsymbol{Y}$ are square matrices. Then, from Corollary 1, it results in

$$\dot{\boldsymbol{u}} = (\boldsymbol{Y}\boldsymbol{M})^{-1}\left(\boldsymbol{C}^{+}\boldsymbol{X}\boldsymbol{J}^T\boldsymbol{c}_{\mathrm{T}} + (\boldsymbol{I} - \boldsymbol{C}^{+}\boldsymbol{C})\boldsymbol{Y}\boldsymbol{c}_{\mathrm{J}}\right) \tag{72}$$

where

$$\boldsymbol{C} \triangleq \boldsymbol{X}\boldsymbol{J}^T\boldsymbol{M}_{\mathrm{T}}\boldsymbol{J}(\boldsymbol{Y}\boldsymbol{M})^{-1} \tag{73}$$

$$\boldsymbol{c}_{\mathrm{T}} \triangleq (\boldsymbol{B}_{\mathrm{T}}\boldsymbol{J} + \boldsymbol{M}_{\mathrm{T}}\boldsymbol{H})\boldsymbol{u} + \boldsymbol{\theta}_{\mathrm{T}}(\boldsymbol{\Phi}(\boldsymbol{q}) \ominus \boldsymbol{p}_r) - \boldsymbol{J}^T\boldsymbol{f}_e \tag{74}$$

$$\boldsymbol{c}_{\mathrm{J}} \triangleq \boldsymbol{B}\boldsymbol{u} + \boldsymbol{\theta}(\boldsymbol{q} - \boldsymbol{q}_r) - \boldsymbol{\tau}_e. \tag{75}$$

Left-multiplying the both sides of (72) by $\boldsymbol{J}^T\boldsymbol{M}_{\mathrm{T}}\boldsymbol{J}$ yields the following:

$$\boldsymbol{J}^T\boldsymbol{M}_{\mathrm{T}}\boldsymbol{J}\dot{\boldsymbol{u}} = -\boldsymbol{X}^{-1}\boldsymbol{C}\boldsymbol{C}^{+}\boldsymbol{X}\boldsymbol{J}^T\boldsymbol{c}_{\mathrm{T}}. \tag{76}$$

Note that the obtained (76) is equivalent to (53) only if

$$\boldsymbol{X}^{-1}\boldsymbol{C}\boldsymbol{C}^{+}\boldsymbol{X}\boldsymbol{J}^T = \boldsymbol{J}^T \tag{77}$$

is satisfied, and the satisfaction of (77) is needed to guarantee the stability of the set $\boldsymbol{\mathcal{X}}_{\mathrm{T}}$ defined in (62) by satisfying $\dot{V}_{\mathrm{T}} \leq 0$. In order to satisfy (77), one sufficient condition is $\boldsymbol{X} = \boldsymbol{Y} = \boldsymbol{M}^{-h}$. This means that the weight matrices need to be chosen to guarantee the stability of the task-space dynamics, and $\boldsymbol{X}^T\boldsymbol{X} = \boldsymbol{Y}^T\boldsymbol{Y} = \boldsymbol{M}^{-1}$ is an appropriate choice.

D. Stability Under Time-Varying References and Time-Varying External Forces

This section analyzes the case where the reference signals $\{\boldsymbol{p}_r, \boldsymbol{f}_r\}$ and the external forces $\{\boldsymbol{f}_s, \boldsymbol{\tau}_s\}$ are time-varying. The analysis here focuses on the local stability around the equilibrium, and is currently restricted to the case under the following assumptions.

1) There exists an equilibrium $\boldsymbol{q} \in \mathbb{R}^n$ satisfying (56) $\wedge$ (57).
2) In the neighborhood of the equilibrium, $\boldsymbol{J}$ is full-rank.

1) In the neighborhood of the equilibrium, the task- and joint-space stiffness terms are not saturated.

These assumptions mean that there exists a $\boldsymbol{q}$ that satisfies the following:

$$\boldsymbol{\Phi}(\boldsymbol{q}) = \boldsymbol{p}_r \oplus \boldsymbol{K}_{\mathrm{T}}^{-1}\boldsymbol{f}_{sr} \tag{78}$$

$$(\boldsymbol{I}_n - \boldsymbol{J}^T\boldsymbol{J}^{\#T})(\boldsymbol{K}(\boldsymbol{q}-\boldsymbol{q}_r) - \boldsymbol{\tau}_s) = \boldsymbol{0}_n. \tag{79}$$

Let us redefine the task-space energy function as follows:

$$V_{\mathrm{T}} \triangleq (\boldsymbol{J}\boldsymbol{u}-\boldsymbol{v}_r)^T\boldsymbol{M}_{\mathrm{T}}(\boldsymbol{J}\boldsymbol{u}-\boldsymbol{v}_r)/2 + (\boldsymbol{\Phi}(\boldsymbol{q}) \ominus \boldsymbol{p}_r)^T\left(\boldsymbol{K}_{\mathrm{T}}(\boldsymbol{\Phi}(\boldsymbol{q}) \ominus \boldsymbol{p}_r)/2 - \boldsymbol{f}_{sr}\right). \tag{80}$$

This function takes its minimum value 0 when $\boldsymbol{J}\boldsymbol{u} = \boldsymbol{v}_r \wedge$ (78). Through tedious but straightforward derivations, its time derivative can be obtained as follows:

$$\begin{aligned}\dot{V}_{\mathrm{T}} =& -(\boldsymbol{J}\boldsymbol{u}-\boldsymbol{v}_r)^T\boldsymbol{B}_{\mathrm{T}}(\boldsymbol{J}\boldsymbol{u}-\boldsymbol{v}_r) - (\boldsymbol{\Phi}(\boldsymbol{q}) \ominus \boldsymbol{p}_r)^T\dot{\boldsymbol{f}}_{sr} \\ & - \boldsymbol{v}_r^T(\boldsymbol{I}_6 - \boldsymbol{J}^{\#T}\boldsymbol{J}^T)\left(\boldsymbol{M}_{\mathrm{T}}(\boldsymbol{H}\boldsymbol{u}-\boldsymbol{a}_r)\right. \\ & \left. + \boldsymbol{B}_{\mathrm{T}}(\boldsymbol{J}\boldsymbol{u}-\boldsymbol{v}_r) + \boldsymbol{K}_{\mathrm{T}}(\boldsymbol{\Phi}(\boldsymbol{q}) \ominus \boldsymbol{p}_r) - \boldsymbol{f}_{sr}\right) \\ =& -(\boldsymbol{J}\boldsymbol{u}-\boldsymbol{v}_r)^T\boldsymbol{B}_{\mathrm{T}}(\boldsymbol{J}\boldsymbol{u}-\boldsymbol{v}_r) - (\boldsymbol{\Phi}(\boldsymbol{q}) \ominus \boldsymbol{p}_r)^T\dot{\boldsymbol{f}}_{sr}.\end{aligned} \tag{81}$$

Here, we used $\boldsymbol{J}\boldsymbol{J}^{\#} = \boldsymbol{I}_6$ based on the full-rank assumption of $\boldsymbol{J}$. The inequality (81) implies that $\dot{V}_{\mathrm{T}} \leq 0$ is satisfied when $\dot{\boldsymbol{f}}_{sr} = \boldsymbol{0}_n$, and $\dot{V}_{\mathrm{T}} = 0$ is satisfied when $\boldsymbol{J}\boldsymbol{u} = \boldsymbol{v}_r \wedge \dot{\boldsymbol{f}}_{sr} = \boldsymbol{0}_n$. The expression (53) implies that the maximum invariant subset of the set satisfying $\boldsymbol{J}\boldsymbol{u} = \boldsymbol{v}_r$ is the set satisfying $\boldsymbol{J}\boldsymbol{u} = \boldsymbol{v}_r \wedge$ (78), in which $V_{\mathrm{T}} = 0$. Therefore, from LaSalle's invariance principle, the set satisfying $\boldsymbol{J}\boldsymbol{u} = \boldsymbol{v}_r \wedge$ (78) is locally asymptotically stable. According to the Lyapunov converse theorem, this local asymptotic stability ensures the existence of a strict Lyapunov function in a neighborhood of this set, and its existence implies the local uniform ultimate boundedness of the state around the set when $\|\dot{\boldsymbol{f}}_{sr}\|$ is small enough. In conclusion, the end-effector position $\boldsymbol{p} = \boldsymbol{\Phi}(\boldsymbol{q})$ tracks the position $\boldsymbol{p}_r \oplus \boldsymbol{K}_{\mathrm{T}}^{-1}\boldsymbol{f}_{sr}$ as long as $\dot{\boldsymbol{f}}_{sr}$ is small enough.

The remaining problem is the convergence of the nullspace dynamics. Unfortunately, the available results require an additional assumption, as follows.

- There exist $\beta > 0$ and $\kappa > 0$ satisfying $\boldsymbol{B} = \beta\boldsymbol{M}$ and $\boldsymbol{K} = \kappa\boldsymbol{M}$, i.e., the joint-space viscosity and stiffness matrices are scalar multiples of the joint-space inertia matrix.

This assumption is made to satisfy $\boldsymbol{J}^T\boldsymbol{J}^{\#T}\boldsymbol{B} = \boldsymbol{B}\boldsymbol{J}^{\#}\boldsymbol{J}$ and $\boldsymbol{J}^T\boldsymbol{J}^{\#T}\boldsymbol{K} = \boldsymbol{K}\boldsymbol{J}^{\#}\boldsymbol{J}$, which are required for the subsequent derivation. This assumption may not be very restrictive in practice because most applications would not require such careful design of the nullspace dynamics.

For notational brevity, let us define $\boldsymbol{\Pi} \triangleq \boldsymbol{I}_n - \boldsymbol{J}\boldsymbol{J}^{\#}$. Then, from (55), one can obtain the following:

$$\boldsymbol{M}\boldsymbol{\Pi}\tilde{\boldsymbol{\alpha}} + \boldsymbol{B}\boldsymbol{\Pi}\tilde{\boldsymbol{u}} + \boldsymbol{K}\boldsymbol{\Pi}\tilde{\boldsymbol{q}} = \boldsymbol{0}_n \tag{82}$$

where $\tilde{\boldsymbol{\alpha}} \triangleq \dot{\boldsymbol{u}} - \boldsymbol{\alpha}_r$, $\tilde{\boldsymbol{u}} \triangleq \boldsymbol{u} - \boldsymbol{u}_r$, and $\tilde{\boldsymbol{q}} \triangleq \boldsymbol{q} - \boldsymbol{q}_r - \boldsymbol{K}^{-1}\boldsymbol{\tau}_s$. It leads to the following expression:

$$\frac{d}{dt}\begin{bmatrix}\boldsymbol{\Pi}\tilde{\boldsymbol{q}}\\ \boldsymbol{\Pi}\tilde{\boldsymbol{u}}\end{bmatrix} = \begin{bmatrix}\boldsymbol{O}_{n\times n} & \boldsymbol{I}_n\\ -\kappa\boldsymbol{M} & -\beta\boldsymbol{M}\end{bmatrix}\begin{bmatrix}\boldsymbol{\Pi}\tilde{\boldsymbol{q}}\\ \boldsymbol{\Pi}\tilde{\boldsymbol{u}}\end{bmatrix} + \begin{bmatrix}\dot{\boldsymbol{\Pi}}\tilde{\boldsymbol{q}} - \boldsymbol{\Pi}\boldsymbol{K}^{-1}\dot{\boldsymbol{\tau}}_s\\ \dot{\boldsymbol{\Pi}}\tilde{\boldsymbol{u}}\end{bmatrix}. \tag{83}$$

Let us define a joint-space energy function as follows:

$$V_{\mathrm{J}} \triangleq \frac{1}{2}\begin{bmatrix}\boldsymbol{\Pi}\tilde{\boldsymbol{q}}\\ \boldsymbol{\Pi}\tilde{\boldsymbol{u}}\end{bmatrix}^T\boldsymbol{P}\begin{bmatrix}\boldsymbol{\Pi}\tilde{\boldsymbol{q}}\\ \boldsymbol{\Pi}\tilde{\boldsymbol{u}}\end{bmatrix} \tag{84}$$

where

$$\boldsymbol{P} \triangleq \begin{bmatrix}\kappa\boldsymbol{M} & (2\kappa\beta/(4\kappa+\beta^2))\boldsymbol{M}\\ (2\kappa\beta/(4\kappa+\beta^2))\boldsymbol{M} & \boldsymbol{M}\end{bmatrix}. \tag{85}$$

Note that $\boldsymbol{P}$ is a symmetric positive-definite matrix. Then, its time derivative can be obtained in the following form:

$$\dot{V}_{\mathrm{J}} = -\begin{bmatrix}\boldsymbol{\Pi}\tilde{\boldsymbol{q}}\\ \boldsymbol{\Pi}\tilde{\boldsymbol{u}}\end{bmatrix}^T\boldsymbol{Q}\begin{bmatrix}\boldsymbol{\Pi}\tilde{\boldsymbol{q}}\\ \boldsymbol{\Pi}\tilde{\boldsymbol{u}}\end{bmatrix} + e \tag{86}$$

where $\boldsymbol{Q}$ is a symmetric positive-definite matrix dependent on κ, β, and $\boldsymbol{M}$, and

$$e \triangleq \begin{bmatrix}\boldsymbol{\Pi}\tilde{\boldsymbol{q}}\\ \boldsymbol{\Pi}\tilde{\boldsymbol{u}}\end{bmatrix}^T\boldsymbol{P}\begin{bmatrix}\dot{\boldsymbol{\Pi}}\tilde{\boldsymbol{q}} - \boldsymbol{\Pi}\boldsymbol{K}^{-1}\dot{\boldsymbol{\tau}}_s\\ \dot{\boldsymbol{\Pi}}\tilde{\boldsymbol{u}}\end{bmatrix}. \tag{87}$$

From the derivation in Appendix C, one has

$$\dot{\boldsymbol{\Pi}} = -\boldsymbol{J}^{\#}\boldsymbol{H}\boldsymbol{\Pi} - \boldsymbol{\Pi}\boldsymbol{M}^{-1}\boldsymbol{H}^T\boldsymbol{J}^{\#T}\boldsymbol{M}. \tag{88}$$

Substituting the above-mentioned into (87) and using the facts $\boldsymbol{\Pi}^T\boldsymbol{M} = \boldsymbol{M}\boldsymbol{\Pi}$ and $\boldsymbol{\Pi}\boldsymbol{J}^{\#} = \boldsymbol{O}_{n\times 6}$, one obtains the following:

$$e = -\begin{bmatrix}\boldsymbol{\Pi}\tilde{\boldsymbol{q}}\\ \boldsymbol{\Pi}\tilde{\boldsymbol{u}}\end{bmatrix}^T\boldsymbol{P}\begin{bmatrix}\boldsymbol{M}^{-1}\boldsymbol{H}^T\boldsymbol{J}^{\#T}\boldsymbol{M}\tilde{\boldsymbol{q}} + \boldsymbol{K}^{-1}\dot{\boldsymbol{\tau}}_s\\ \boldsymbol{M}^{-1}\boldsymbol{H}^T\boldsymbol{J}^{\#T}\boldsymbol{M}\tilde{\boldsymbol{u}}\end{bmatrix}. \tag{89}$$

The inequality (86) implies that $\dot{V}_{\mathrm{J}} \leq 0$ is satisfied as long as e is small enough, and (89) implies that e is small when $\boldsymbol{H}$ and $\dot{\boldsymbol{\tau}}_s$ are small. Considering the definition of $\boldsymbol{H}$, $\boldsymbol{H}$ at the equilibrium is small when $\boldsymbol{u}_r$ and $\boldsymbol{v}_r$ are small. Therefore, one can see that the set $\boldsymbol{\Pi}\tilde{\boldsymbol{q}} = \boldsymbol{0}_n \wedge \boldsymbol{\Pi}\tilde{\boldsymbol{u}} = \boldsymbol{0}_n$ is asymptotically stable if $\dot{\boldsymbol{\tau}}_s$, $\boldsymbol{u}_r$, and $\boldsymbol{v}_r$ are sufficiently small, implying that the nullspace motion eventually settles.

The analysis presented here is built on some restrictive assumptions, and the obtained result only concerns local stability. The relaxation of these assumptions, the clarification of upper bounds for $\|\dot{\boldsymbol{f}}_{sr}\|$, $\|\dot{\boldsymbol{\tau}}_s\|$, $\|\boldsymbol{u}_r\|$, and $\|\boldsymbol{v}_r\|$, as well as the characterization of the region of attraction, still remain open problems.

VI. Experiments

A. Experimental Setup

The proposed method was tested with an experimental setup shown in Fig. 5, which is a Kinova Gen3 robot. It has seven joints equipped with torque sensors. The robot was connected to a PC running Windows OS, and the controllers for the robot were constructed with Microsoft Visual C++. The sampling interval of

IEEE Transactions on Robotics (T-RO) paper, presented at ICRA 2026, Vienna, Austria. Cite as T-RO paper.

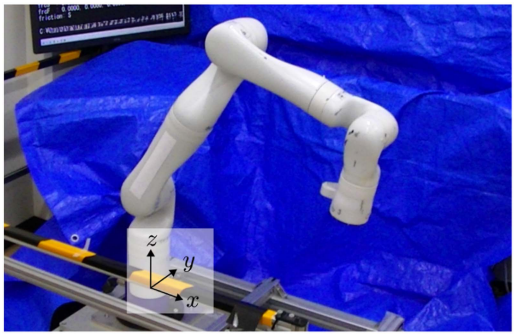

Fig. 5. Experimental setup (Kinova Gen 3).

$T = 0.001$ s was realized with `QueryPerformanceCouner` function of Win32 API.

The proposed controller, which is the algorithm (18) with the function TwoProxies in (36) and the function SatPosCtrl in (16), was implemented to the PC. The basic settings for the controller parameters were chosen following the guidelines outlined in Section IV-D. More specifically, the following procedure was used. First, the torque limits F_c for the joints were set as 80 % of the maximum torque [35]; $F_c = 43.2\,\mathrm{Nm}$ for the first four joints and $F_c = 27.2\,\mathrm{Nm}$ for the other joints. Second, the proxy dynamics were disabled [i.e., $\boldsymbol{q}_x^*$ in (18) was kept constant], and the gain values (K_c, B_c, and L_c) for the function SatPosCtrl were chosen so that the joint angles were stiffly maintained at $\boldsymbol{q}_x^*$. Through some trial and error, they were chosen as $\{K_c, B_c, L_c\} = \{1500\,\mathrm{Nm},\ 30\,\mathrm{Nms},\ 300\,\mathrm{Nm/s}\}$ for the first four joints and $\{1000\,\mathrm{Nm},\ 20\,\mathrm{Nms},\ 200\,\mathrm{Nm/s}\}$ for the other joints. Third, the task-space proxy dynamics was disabled by overwriting $\boldsymbol{C}_{\mathrm{TJ}}^{+} := \boldsymbol{O}_{7\times 7}$ in the function TwoProxies, and the joint-space proxy parameters were chosen to realize stable joint-independent admittance control, resulting in

$$\boldsymbol{M} = \mathrm{diag}\,[1.5, 1.2, 0.8, 0.8, 0.4, 0.4, 0.4]\,\mathrm{kg{\cdot}m^2} \tag{90a}$$

$$\boldsymbol{B} = (2\,\mathrm{s}^{-1}) \times \boldsymbol{M} \tag{90b}$$

$$\boldsymbol{K} = (1\,\mathrm{s}^{-2}) \times \boldsymbol{M} \tag{90c}$$

which realizes critical damping with the time constant of 1 s. The force limits for the joint-space proxy springs were set as

$$\boldsymbol{F} = [30, 30, 30, 30, 20, 20, 20]^T\,\mathrm{Nm}. \tag{91}$$

The reference position for the joint-space proxy was set as follows:

$$\boldsymbol{q}_r \equiv [0, 0, 0, 0, 0, 0, 0]^T\,\mathrm{rad}. \tag{92}$$

Finally, the task-space proxy parameters were chosen to realize stable task-space admittance control. Some preliminary experiments resulted in

$$\boldsymbol{M}_{\mathrm{T}} = \mathrm{blockdiag}\,[(2.5\,\mathrm{kg}) \times \boldsymbol{I}_3, (0.25\,\mathrm{kg{\cdot}m^2}) \times \boldsymbol{I}_3] \tag{93a}$$

$$\boldsymbol{B}_{\mathrm{T}} = (4\,\mathrm{s}^{-1}) \times \boldsymbol{M}_{\mathrm{T}} \tag{93b}$$

$$\boldsymbol{K}_{\mathrm{T}} = (4\,\mathrm{s}^{-2}) \times \boldsymbol{M}_{\mathrm{T}} \tag{93c}$$

which realizes critical damping with the time constant of 0.5 s. The force limit for the task-space proxy spring was set as

$$\boldsymbol{F}_{\mathrm{T}} = [100\,\mathrm{N},\ 10\,\mathrm{Nm}]^T. \tag{94}$$

Unless otherwise noted, the reference position for the task-space proxy was set as

$$\boldsymbol{p}_r \equiv [0.5\,\mathrm{m}, 0\,\mathrm{m}, 0.4\,\mathrm{m}, 0, 0, 1, 0]^T \tag{95}$$

and the reference force was set as $\boldsymbol{f}_r \equiv \boldsymbol{0}_6$.

In the function TwoProxies, the pseudoinverse $\boldsymbol{C}_{\mathrm{TJ}}^{+}$ was replaced by the continualized pseudoinverse $\boldsymbol{C}_{\mathrm{TJ}}^{\oplus}$, detailed in Section IV-C, where the parameter ε was chosen as $\varepsilon = 0.03$. It was chosen as small as possible without causing oscillations when the robot was fully stretched.

The gravity compensation was performed by computing the gravity torques from the mass parameters of the links provided in [35]. The computed gravity torques were superposed to the output $\boldsymbol{\tau}_m$ of the controller (18).

To investigate the necessity of individual components of the proposed controller, some ablated versions of the proposed controller were compared, which are as follows.

1) Controller **C1**: A controller in which the function SatPosCtrl was replaced by an ordinary torque-saturated PID controller, i.e., with the line (16e) being replaced by $q_x := q^*$. It means that its internal position controller was a PID controller that saturates the torque without maintaining consistency with the proxy position $\boldsymbol{q}_x$. This controller was employed to illustrate the proposed controller's capability of handling actuator torque saturation.
2) Controller **C2**: A controller with the velocity projection being disabled, with the line (18e) removed from the algorithm (18). It is to illustrate the necessity of the velocity-projecting operation, without which the controller would have been simpler.
3) Controller **C3**: A controller with the continualized pseudoinverse $\boldsymbol{C}_{\mathrm{TJ}}^{\oplus}$ being replaced by the damped approximation of $\boldsymbol{C}_{\mathrm{TJ}}^{+}$ in (39). It is to illustrate the effect of the continualized pseudoinverse $\boldsymbol{C}_{\mathrm{TJ}}^{\oplus}$. The parameter values $\varepsilon_x = \varepsilon_s = 0.004$ were chosen through some preliminary experiments so that they were as small as possible without causing oscillations when the robot was fully stretched.

Controllers dependent on the robot's dynamics model, such as those in [17], [20], and [22], were not included in the empirical comparison because the performance of such controllers would depend on the accuracy of the model. Being free from an explicit dynamics model can count as an advantage of the proposed controller, particularly for robots with highly frictional joints and complex dynamics. Admittance controllers for position-commanded or velocity-commanded robots, such as those in [18], [19], [23], and [36], were not experimentally compared either because they are inherently incapable of dealing with the actuator torque saturation.

Videos of the following experiments are included in the multimedia attachment of this article.

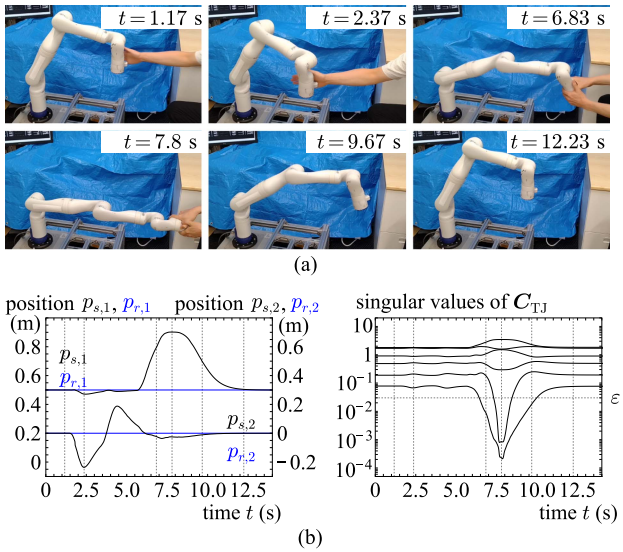

Fig. 6. Experiment IA. (a) Snapshots. (b) End-effector position in x and y directions and the singular values of $\boldsymbol{C}_{\mathrm{TJ}}$. (The vertical lines in the graphs correspond to the snapshots).

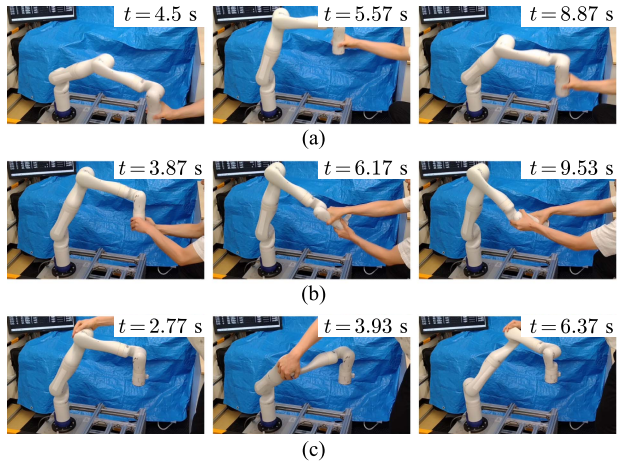

Fig. 7. Snapshots of (a) Experiment IB, (b) Experiment IC, and (c) Experiment ID.

B. Experiments IA to ID: Moved by Hand

The first set of experiments was conducted to validate the task-space admittance control realized by the proposed method. As an Experiment IA, the experimenter performed the maneuver shown by the snapshots in Fig. 6(a), which is divided into the following periods.

1) **Period A** ($t \in [0\,\mathrm{s},\ 6\,\mathrm{s}]$): The experimenter lightly pushed the end-effector right and left, in the y direction, by his palm, without holding it.
2) **Period B** ($t \in [6\,\mathrm{s},\ 9\,\mathrm{s}]$): The experimenter pulled the end-effector in the $+x$ direction.
3) **Period C** ($t \in [9\,\mathrm{s},\ 14\,\mathrm{s}]$): The experimenter removed his hand from the end-effector.

Fig. 6(b) shows the singular values of the matrix $\boldsymbol{C}_{\mathrm{TJ}}$ during the maneuver.

As can be seen in Fig. 6(a), in period A, the end-effector moved horizontally almost along a straight line without changing the attitude, although the experimenter did not attempt to hold it at a fixed attitude. It indicates the validity of the task-space dynamics realized by the proposed controller. In Period B, the robot came into a singular configuration, and some singular values became smaller, as in Fig. 6(b). It indicates that the controller tolerates the singular configuration. In period C, the robot returned to the original position, which was the reference position $\boldsymbol{p}_r$, indicating the spring term in the task-space proxy dynamics (20) worked properly.

Additional trials were performed with different parameter settings. As an Experiment IB, the rotational components of $\{\boldsymbol{M}_{\mathrm{T}}, \boldsymbol{B}_{\mathrm{T}}, \boldsymbol{K}_{\mathrm{T}}, \boldsymbol{F}_{\mathrm{T}}\}$ were scaled by 1000 from the values in (93), and the experimenter moved the end-effector randomly around the initial position. As seen in Fig. 7(a), the end-effector was moved without changing its attitude, indicating the validity of the task-space dynamics realized by the proposed controller.

As an Experiment IC, the translational components of $\{\boldsymbol{M}_{\mathrm{T}}, \boldsymbol{B}_{\mathrm{T}}, \boldsymbol{K}_{\mathrm{T}}, \boldsymbol{F}_{\mathrm{T}}\}$ were scaled by 1000 from the values in (93), and the experimenter attempted to rotate the end-effector randomly. As seen in Fig. 7(b), the end-effector changed its attitude without changing its position. It should be emphasized that it even passed through the wrist singular configuration, as can be seen in $t = 6.17$ s of Fig. 7(b). This behavior indicates that the controller properly realizes the rotational dynamics and maintains validity even in singular configurations.

As an Experiment ID, all elements of $\{\boldsymbol{M}_{\mathrm{T}}, \boldsymbol{B}_{\mathrm{T}}, \boldsymbol{K}_{\mathrm{T}}, \boldsymbol{F}_{\mathrm{T}}\}$ were scaled by 1000 from the values in (93), and the experimenter pushed the elbow joint of the robot. As seen in Fig. 7(c), the robot moved only its elbow part without moving the end-effector, indicating the validity of the nullspace dynamics realized by the proposed controller.

C. Experiment II: Behavior Under Torque Saturation

Another set of experiments was performed to test the effect of torque saturation. In this experiment, the parameter F_c, which determines the saturation level of each joint torque, was set to be 30% of each value indicated in Section VI-A. The task-space proxy parameters $\{\boldsymbol{M}_{\mathrm{T}}, \boldsymbol{B}_{\mathrm{T}}, \boldsymbol{K}_{\mathrm{T}}, \boldsymbol{F}_{\mathrm{T}}\}$ were scaled by the factor 1000 from the values in (93) except those in the y direction so that the end-effector motion was guided along the y direction. The robot was initially set at $\boldsymbol{p}_r$ in (95), and the experimenter moved the end-effector left and right, in the y-direction, by holding it by hand.

Experiments were performed with three controllers: the proposed controller and controllers **C1** and **C2** introduced in Section VI-A. Fig. 8(a) shows the results of the proposed controller; the measured position $\boldsymbol{p}_s$, the task-space proxy position $\boldsymbol{p}_x$, the reference position $\boldsymbol{p}_r$, and the command torque $\tau_{m,1}$ of the base (first) joint. It is shown that the torque $\tau_{m,1}$ was saturated but the proxy position $\boldsymbol{p}_x$ remained close to the measured position $\boldsymbol{p}_s$, resulting in stable behavior. In fact, after $t = 7$ s when the experimenter removed the hand from the robot, the robot reached a settled state.

Fig. 8(b) shows the results of controller **C1**, in which the function SatPosCtrl was replaced by an ordinary torque-saturated PID controller. Also in this trial, the experimenter held the end-effector and attempted to move it left and right, in the

IEEE Transactions on Robotics (T-RO) paper, presented at ICRA 2026, Vienna, Austria. Cite as T-RO paper.

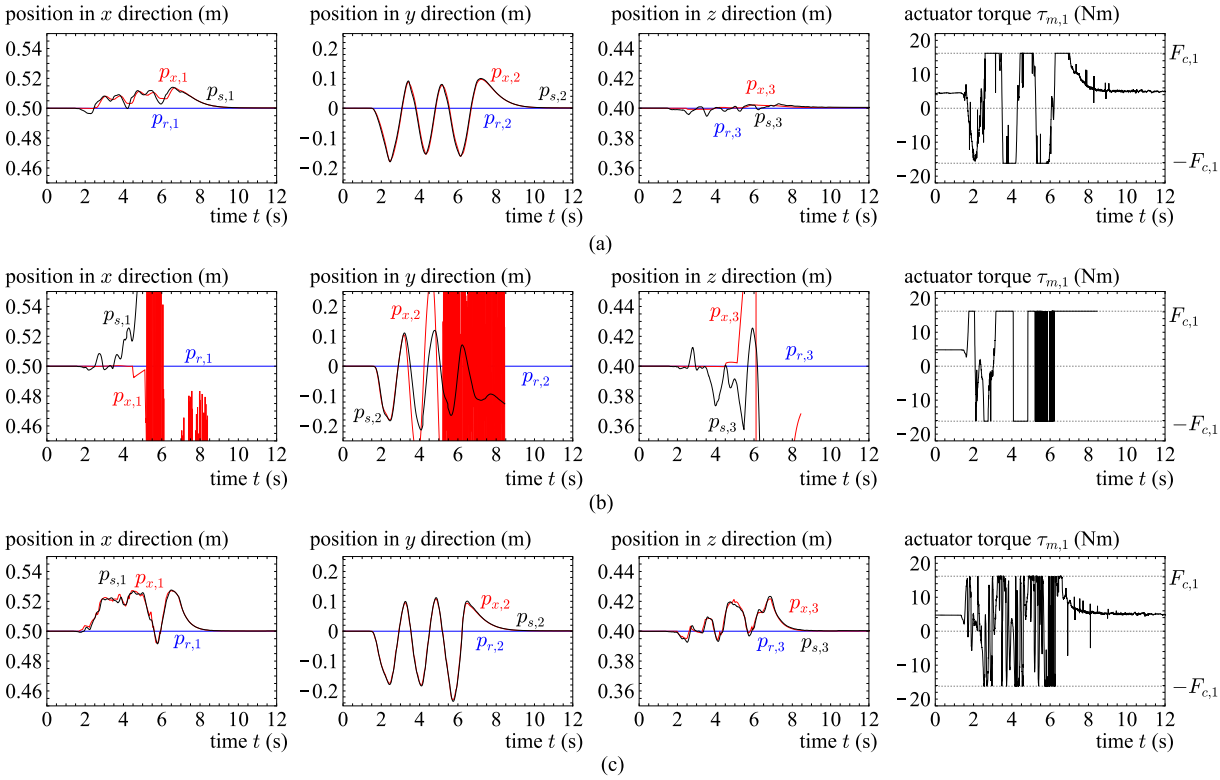

Fig. 8. Results of Experiment II. (a) Proposed controller. (b) Controller **C1**, with the function SatPosCtrl being replaced by an ordinary torque-saturated PID controller. (c) Controller **C2**, with the velocity projection being disabled. Note that the scales of the x- and z-position graphs are magnified by a factor of 5 from that of the y-position.

y-direction. It can be seen from the figure that, once the torques were saturated, the proxy position $\boldsymbol{q}_x$ deviated from the actual position $\boldsymbol{q}_s$. In this case, the experimenter's hand was pulled by the force swinging around unpredictably, and he had to grasp the end-effector tightly to prevent unsafe motion. The experimenter eventually had to stop the robot at $t = 8.5$ s to prevent further violent behaviors.

Fig. 8(c) shows the results of controller **C2**, in which the velocity projection was disabled. Although it is not apparent from the figure, the experimenter felt a lighter resistance from the robot than in the case with the proposed controller, and also felt a pulling force in unpredictable directions from the robot. In fact, controller **C2** resulted in larger positional errors in the x- and z-direction from the reference position $\boldsymbol{p}_r$ than the proposed method, as can be seen from the figure.

These results suggest that the proposed controller properly inherits the beneficial properties of TBAC, as seen in Fig. 8(a), and it is effective in preventing such undesirable, unsafe behaviors seen in Fig. 8(b). The velocity projection can also be said to be desirable for enhancing safety and accuracy under torque saturation, as can be seen in Fig. 8(c).

D. Experiment III: Trajectory Tracking With Disturbance on Elbow

Experiment III was conducted to test the trajectory tracking capability of the proposed controller. A time-varying reference $\boldsymbol{p}_r(t)$ for the end-effector position was given to the controller, which was a sinusoidal trajectory between the two positions $\boldsymbol{p}_{rA} \in \mathbb{P}$ and $\boldsymbol{p}_{rB} \in \mathbb{P}$ shown in Fig. 9(a). Specifically, the reference position $\boldsymbol{p}_r(t)$ was given as follows:

$$\boldsymbol{p}_r(t) = \boldsymbol{p}_{rA} \oplus \left(\frac{1 - \cos(2\pi t/T_{\mathrm{S}})}{2} (\boldsymbol{p}_{rB} \ominus \boldsymbol{p}_{rA}) \right) \tag{96}$$

where $T_{\mathrm{S}} = 4$ s. The parameters $\{\boldsymbol{M}_{\mathrm{T}}, \boldsymbol{B}_{\mathrm{T}}, \boldsymbol{K}_{\mathrm{T}}, \boldsymbol{F}_{\mathrm{T}}\}$ for the task-space proxy were scaled by the factor of 1000 from the values in (93). In the middle of the motion, the experimenter applied a pushing force on the elbow part of the robot, as shown in the right-most snapshot in Fig. 9(a).

The results are shown in Fig. 9(b), which shows the x component of the end-effector position and the angle $q_{s,1}$ of the first joint. One can see that the trajectory tracking of the end-effector was properly realized, allowing the nullspace motion (seen in the first joint motion) according to the external force. Despite the large displacement of the first joint, the end-effector trajectory was not much disturbed. In addition, the displaced first joint returns to the original position after the experimenter's hand was removed, which can be attributed to the joint-space proxy spring.

Controller **C3**, with the damped pseudoinverse in (39), was also tested in the same experimental procedure, and the results are shown in Fig. 9(c). It shows that Controller **C3** resulted in a slightly larger tracking error than that of the proposed controller. Fig. 9(d) compares the tracking error $\|\boldsymbol{p}_{s,1:3} - \boldsymbol{p}_{r,1:3}\|$ between the two controllers, showing that controller **C3** indeed resulted in larger tracking error than the proposed controller. It can be

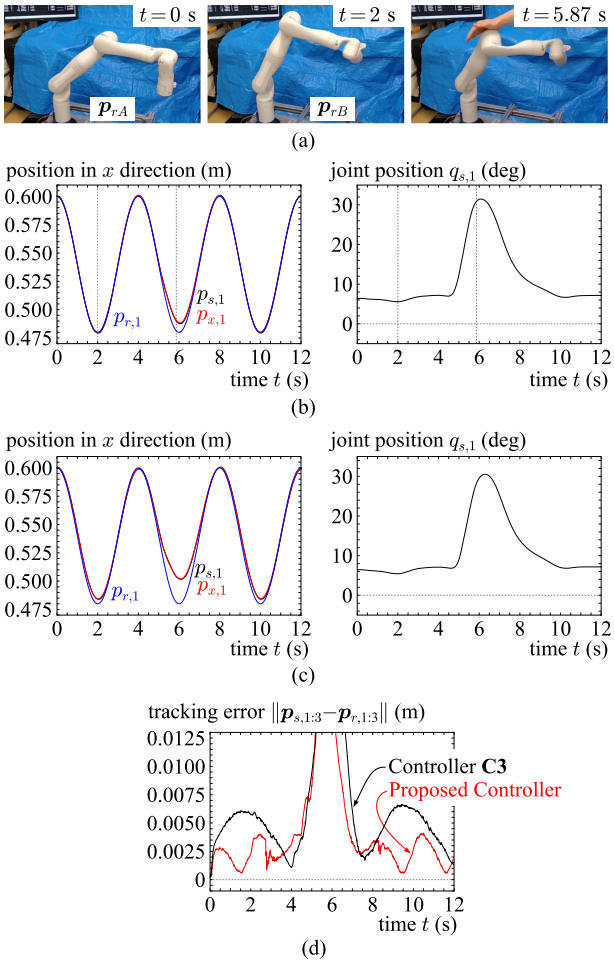

Fig. 9. Experiment III. (a) Snapshots of two reference positions, $\boldsymbol{p}_{rA}$ and $\boldsymbol{p}_{rB}$, and how the elbow was pushed by the experimenter. (b) Results of the proposed controller. (c) Results of controller **C3**. (d) Comparison of tracking errors. Note that the errors in $t \in [5\,\mathrm{s}, 8\,\mathrm{s}]$ were caused by the external force intentionally applied by the experimenter's hand, which may have varied across trials.

attributed to the fact that the damped pseudoinverse produces a certain level of inaccuracy even when it is away from the singularity, while the proposed continualized pseudoinverse does not.

E. Experiment IV: Contact Force Control

Experiment IV was performed to test the capability of the proposed controller in the contact force control. As a contact environment, a cardboard box was placed below the end-effector, as shown in Fig 10(a). The reference force was set as $\boldsymbol{f}_r = [0, 0, f_{r,3}, 0, 0, 0]^T$ and $f_{r,3}$, which is the z component of the translational reference force, was varied in a step-like manner among 0, 10, and 20 N. To prevent oscillation that happened in preliminary experiments involving the environment contact, all elements of $\{\boldsymbol{M}_\mathrm{T}, \boldsymbol{B}_\mathrm{T}, \boldsymbol{K}_\mathrm{T}, \boldsymbol{F}_\mathrm{T}\}$ were scaled by 20 from the values in (93) except the (3, 3)-th element of $\boldsymbol{K}_\mathrm{T}$ being set zero.

The results are shown in Fig. 10(b). The graph shows the third element (z component) of the force vector $\boldsymbol{f}_s = \boldsymbol{J}(\boldsymbol{q}_s)^{+}\boldsymbol{\tau}_s$. The results show that the contact force $f_{s,3}$ appropriately tracked the

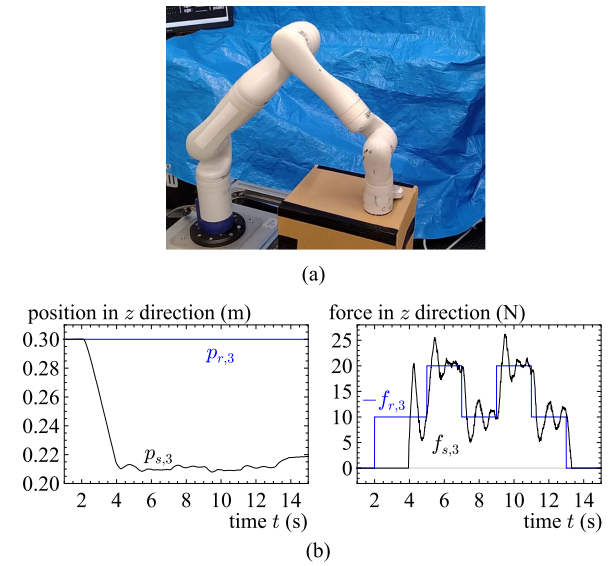

Fig. 10. Experiment IV. (a) Robot pushing the contact environment. (b) Contact force and reference force in the z-direction.

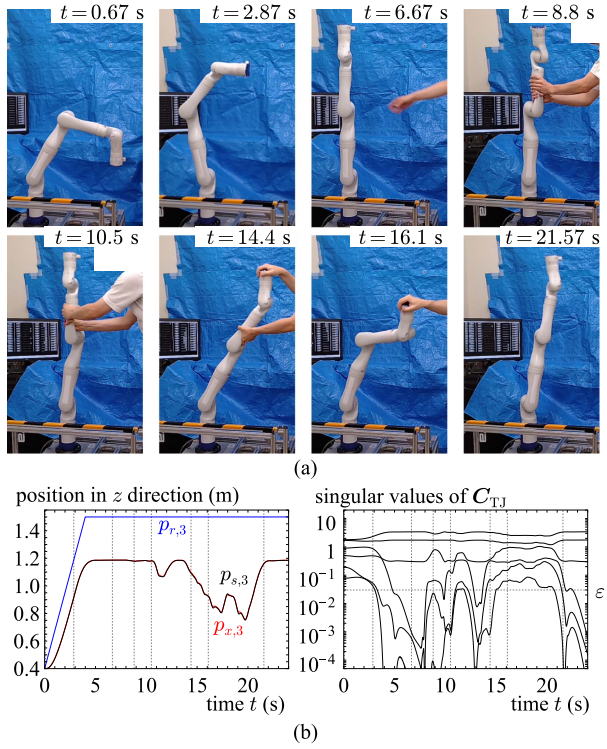

Fig. 11. Experiment V. (a) Snapshots. (b) End-effector position in z-direction and the singular values of $\boldsymbol{C}_{\mathrm{TJ}}$. (The vertical lines in the graphs correspond to the snapshots).

negative of the reference force $-f_{r,3}$, showing the applicability of the proposed admittance controller as a contact force controller.

F. Experiment V: Unreachable Reference Position

Experiment V was performed to test the controller's response to the reference position $\boldsymbol{p}_r$ set outside the reachable workspace.

The reference position $\boldsymbol{p}_r$ was initial set as (95) and was linearly moved to $\boldsymbol{p}_r = [0\,\mathrm{m}, 0\,\mathrm{m}, 1.5\,\mathrm{m}, 1, 0, 0, 0]^T$ from $t = 0$ s to $t = 5$ s. This $\boldsymbol{p}_r$ represents a position right above the robot base with an upward-pointing attitude, located outside the robot's reachable workspace. After $t = 10$ s, the experimenter applied some forces on the end-effector and the links.

Fig. 11(a) shows some snapshots of this experiment and Fig. 11(b) shows the temporal changes of the end-effector positions and the singular values of $\boldsymbol{C}_{\mathrm{TJ}}$. It can be seen that the robot reached an equilibrium at a configuration pointing straight upward around $t = 5$ s. After this, three of the singular values of $\boldsymbol{C}_{\mathrm{TJ}}$ were below the threshold ε. Between $t = 8$ s and $t = 11$ s, the experimenter was able to twist the middle links, indicating the validity of the joint-space dynamics realized in the nullspace. Then, the experimenter moved the end-effector by lightly holding it, and the end-effector moved without much change in the end-effector attitude, exhibiting the validity of the task-space admittance control. After the experimenter removed his hand from the robot, the robot returned to the upward-pointing attitude, indicating the proper realization of the effect of the task-space proxy spring.

VII. Conclusion

This article has proposed a task-space version of TBAC that tolerates singular configurations and can be used with redundant manipulators. It imposes an explicit torque limit to each joint without causing undesirable or unsafe side effects, while it enforces that the end-effector follows predefined task-space proxy dynamics as long as the joint torques are unsaturated and the robot is out of the singular configurations. The behavior of the robot in the nullspace is determined by predefined joint-space proxy dynamics. The task- and joint-space proxy dynamics are combined through a newly proposed continualized pseudoinverse, which is an alternative approximation of the pseudoinverse matrix. The controller was validated through experiments with a seven-DOF Kinova Gen3 robot. The results illustrate that the proposed controller acts as a proper task-space admittance controller that safely handles actuator force saturation and singular configurations, and also as a contact force controller and a trajectory-tracking controller. It was also shown that the proposed method with the continualized pseudoinverse realizes higher accuracy in trajectory tracking than the case with a damped pseudoinverse.

An important open problem is to establish appropriate guidelines for parameter tuning. In particular, deeper theoretical and empirical studies would be needed to clarify the effect of the threshold ε for the continualized pseudoinverse. In addition, it is important to analyze the combined task-space and joint-space dynamics in more detail. The analysis in this article assumed that the joint-space inertia, viscosity, and stiffness matrices are scalar multiples of each other, but this assumption should be reconsidered or preferably removed. A more in-depth analysis under conditions of torque saturation and time-varying references should also be conducted.

Appendix A
Quaternion Calculus

The attitude of a rigid body in the Cartesian space can be represented by a 3×3 rotation matrix ($\in \mathrm{SO}(3)$) whose column vectors represent the axes of the body-fixed frame. A unit quaternion can also represent the attitude of a rigid body. A unit quaternion $\boldsymbol{a} = [a_w, a_x, a_y, a_z]^T \in \mathbb{H}$ to its correspondent 3×3 rotation matrix can be associated by the following map:

$$\mathrm{q2m}(\boldsymbol{a}) \triangleq \begin{bmatrix} a_w^2 + a_x^2 - a_y^2 - a_z^2 & 2(a_x a_y - a_w a_z) & 2(a_x a_z + a_w a_y) \\ 2(a_x a_y + a_w a_z) & a_w^2 - a_x^2 + a_y^2 - a_z^2 & 2(a_y a_z - a_w a_x) \\ 2(a_x a_z - a_w a_y) & 2(a_y a_z + a_w a_x) & a_w^2 - a_x^2 - a_y^2 + a_z^2 \end{bmatrix}.$$

We define the time derivative operator $\circ$ for a unit quaternion $\boldsymbol{a} = [a_w, a_x, a_y, a_z]^T$ as follows:

$$\mathring{\boldsymbol{a}} \triangleq 2 \begin{bmatrix} -a_x & a_w & -a_z & a_y \\ -a_y & a_z & a_w & -a_x \\ -a_z & -a_y & a_x & a_w \end{bmatrix} \begin{bmatrix} \dot{a}_w \\ \dot{a}_x \\ \dot{a}_y \\ \dot{a}_z \end{bmatrix}. \tag{97}$$

Note that $\boldsymbol{a} \in \mathbb{H}$ and $\mathring{\boldsymbol{a}} \in \mathbb{R}^3$. With this operator, the angular velocity $\boldsymbol{\omega} \in \mathbb{R}^3$ and the attitude $\boldsymbol{a} \in \mathbb{H}$ of a rigid body can be associated as $\boldsymbol{\omega} = \mathring{\boldsymbol{a}}$.

Now we prepare some operators to relate the discrete-time representations of the attitude quaternions and the angular velocity vectors. First, the quaternion multiplication $\otimes : \mathbb{H} \times \mathbb{H} \to \mathbb{H}$ is defined as follows:

$$\begin{bmatrix} a_w \\ a_x \\ a_y \\ a_z \end{bmatrix} \otimes \begin{bmatrix} b_w \\ b_x \\ b_y \\ b_z \end{bmatrix} \triangleq \begin{bmatrix} a_w b_w - a_x b_x - a_y b_y - a_z b_z \\ a_x b_w + a_w b_x - a_z b_y + a_y b_z \\ a_y b_w + a_z b_x + a_w b_y - a_x b_z \\ a_z b_w - a_y b_x + a_x b_y + a_w b_z \end{bmatrix}.$$

Based on this, let the operators $\ominus : \mathbb{H} \times \mathbb{H} \to \mathbb{R}^3$ and $\oplus : \mathbb{H} \times \mathbb{R}^3 \to \mathbb{H}$ be defined as follows:[3]

$$\boldsymbol{a} \ominus \boldsymbol{b} \triangleq \mathrm{q2v}\,(\boldsymbol{a} \otimes \mathrm{inv}(\boldsymbol{b})) \tag{98}$$

$$\boldsymbol{a} \oplus \boldsymbol{r} \triangleq \mathrm{v2q}(\boldsymbol{r}) \otimes \boldsymbol{a} \tag{99}$$

where $\mathrm{inv} : \mathbb{H} \to \mathbb{H}$, $\mathrm{q2v} : \mathbb{H} \to \mathbb{R}^3$, and $\mathrm{v2q} : \mathbb{R}^3 \to \mathbb{H}$ are defined as follows:

$$\mathrm{inv}\left(\begin{bmatrix} a_w \\ \boldsymbol{a}_{xyz} \end{bmatrix}\right) \triangleq \begin{bmatrix} a_w \\ -\boldsymbol{a}_{xyz} \end{bmatrix} \tag{100}$$

$$\mathrm{q2v}\left(\begin{bmatrix} a_w \\ \boldsymbol{a}_{xyz} \end{bmatrix}\right) \triangleq \frac{2\,\mathrm{sgn}(a_w)}{\mathrm{sinc}\,(\mathrm{asin}(\|\boldsymbol{a}_{xyz}\|))} \boldsymbol{a}_{xyz} \tag{101}$$

$$\mathrm{v2q}\,(\boldsymbol{r}) \triangleq \begin{bmatrix} \cos(\|\boldsymbol{r}\|/2) \\ \boldsymbol{r}\,\mathrm{sinc}(\|\boldsymbol{r}\|/2)/2 \end{bmatrix}. \tag{102}$$

The functions q2v and v2q are to associate a unit quaternion to its correspondent rotation vector. With $\boldsymbol{a} \in \mathbb{H}$, $\boldsymbol{b} \in \mathbb{H}$, and

[3]The definitions of these notations are equivalent to those in [37], but different from those in [38]. In our definitions, the attitude $\boldsymbol{a} \oplus \boldsymbol{r}$ is the attitude $\boldsymbol{a}$ rotated by $\boldsymbol{r}$ seen from the world frame, but in [38], it is by $\boldsymbol{r}$ seen from the body frame. Similar notations are also found in [39] and [40].

$\boldsymbol{r} \in \mathbb{R}^3$, the operators $\ominus$ and $\oplus$ satisfy the following relation:

$$\boldsymbol{a} \ominus \boldsymbol{b} = \boldsymbol{r} \iff \boldsymbol{a} = \boldsymbol{b} \oplus \boldsymbol{r} \quad \text{if } \|\boldsymbol{r}\| < \pi \tag{103}$$

which can be shown through tedious but straightforward derivations.

With the operator $\ominus$, the following relation holds true:

$$\lim_{T\to 0} \frac{(\boldsymbol{a} + T\dot{\boldsymbol{a}}) \ominus \boldsymbol{a}}{T} = \mathring{\boldsymbol{a}}. \tag{104}$$

From (104), the backward Euler discretization of the relation $\boldsymbol{\omega} = \mathring{\boldsymbol{a}}$ between the attitude $\boldsymbol{a} \in \mathbb{H}$ and the angular velocity $\boldsymbol{\omega} \in \mathbb{R}^3$ can be given as follows:

$$\boldsymbol{\omega} = (\boldsymbol{a} \ominus \boldsymbol{a}_{\text{prv}})/T, \quad \boldsymbol{a} = \boldsymbol{a}_{\text{prv}} \oplus T\boldsymbol{\omega} \tag{105}$$

where T is the timestep size and $\boldsymbol{a}_{\text{prv}}$ is the value of $\boldsymbol{a}$ in the previous timestep. The expression (105) is particularly convenient due to its representational similarity to the backward-Euler discretization of vector quantities in ordinary vector spaces, such as translational positions or velocities. Moreover, these operators can be implemented by overloading the operators "$-$" and "$+$" in the C++ language. It should be noted, however, that the operator "$\oplus$" is not commutative, unlike its counterpart "$+$" in ordinary vector spaces.

In order to deal with the position and the attitude of a rigid body in brief expressions, we define the set $\mathbb{P} \triangleq \mathbb{R}^3 \times \mathbb{H}$ and redefine the operators $\ominus : \mathbb{P} \times \mathbb{P} \to \mathbb{R}^6$ and $\oplus : \mathbb{P} \times \mathbb{R}^6 \to \mathbb{P}$ as follows:

$$\begin{bmatrix} \boldsymbol{r}_1 \\ \boldsymbol{a}_1 \end{bmatrix} \ominus \begin{bmatrix} \boldsymbol{r}_2 \\ \boldsymbol{a}_2 \end{bmatrix} \triangleq \begin{bmatrix} \boldsymbol{r}_1 - \boldsymbol{r}_2 \\ \boldsymbol{a}_1 \ominus \boldsymbol{a}_2 \end{bmatrix} \tag{106}$$

$$\begin{bmatrix} \boldsymbol{r}_1 \\ \boldsymbol{a}_1 \end{bmatrix} \oplus \begin{bmatrix} \boldsymbol{r}_2 \\ \boldsymbol{r}_3 \end{bmatrix} \triangleq \begin{bmatrix} \boldsymbol{r}_1 + \boldsymbol{r}_2 \\ \boldsymbol{a}_1 \oplus \boldsymbol{r}_3 \end{bmatrix} \tag{107}$$

where $\boldsymbol{r}_* \in \mathbb{R}^3$ and $\boldsymbol{a}_* \in \mathbb{H}$. Note that $\mathbb{P}$ can be seen as an alternative representation of $\mathrm{SE}(3)$. The operators "$\ominus$" and "$\oplus$" defined with $\mathbb{P}$ and $\mathbb{R}^6$ allow concise representations of the Euler discretizations of translational and rotational equations of motion. In addition, we define the time derivative operator "$\circ$" for $\boldsymbol{p} = [\boldsymbol{r}^T, \boldsymbol{a}^T]^T \in \mathbb{P}$ as follows:

$$\mathring{\boldsymbol{p}} \triangleq [\dot{\boldsymbol{r}}^T, \mathring{\boldsymbol{a}}^T]^T \in \mathbb{R}^6. \tag{108}$$

It should be emphasized that $\boldsymbol{p} \in \mathbb{P}$ and $\mathring{\boldsymbol{p}} \in \mathbb{R}^6$.

Now let us consider an n-DOF rigid-link manipulator with a single end-effector. Let $\boldsymbol{q} \in \mathbb{R}^n$ be the joint variable vector of the manipulator, and $\boldsymbol{p} \in \mathbb{P}$ be the position and the attitude of the end-effector. Let $\boldsymbol{u} \in \mathbb{R}^n$ be the joint velocity vector defined as $\boldsymbol{u} = \dot{\boldsymbol{q}}$ and $\boldsymbol{v} \in \mathbb{R}^6$ be the vector of the translational velocity and the angular velocity of the end-effector, which satisfies $\boldsymbol{v} = \mathring{\boldsymbol{p}}$. With the forward kinematics $\boldsymbol{\Phi} : \mathbb{R}^n \to \mathbb{P}$ of the manipulator, we have $\boldsymbol{p} = \boldsymbol{\Phi}(\boldsymbol{q})$. We can define the Jacobian of $\boldsymbol{\Phi}$ based on the operator $\ominus$, which is defined as the function $\boldsymbol{J} : \mathbb{R}^n \to \mathbb{R}^{6\times n}$ satisfying the following:

$$\boldsymbol{J}(\boldsymbol{q})\boldsymbol{u} = \lim_{T\to 0} \frac{\boldsymbol{\Phi}(\boldsymbol{q} + T\boldsymbol{u}) \ominus \boldsymbol{\Phi}(\boldsymbol{q})}{T} \quad \forall \boldsymbol{u} \in \mathbb{R}^n. \tag{109}$$

With such a function $\boldsymbol{J}$, we can relate the velocities $\boldsymbol{v} \in \mathbb{R}^n$ and $\boldsymbol{u} \in \mathbb{R}^6$ by $\boldsymbol{v} = \boldsymbol{J}(\boldsymbol{q})\boldsymbol{u}$. Moreover, with the backward Euler discretization $\boldsymbol{u} = (\boldsymbol{q} - \boldsymbol{q}_{\text{prv}})/T$, we have

$$(\boldsymbol{\Phi}(\boldsymbol{q}) \ominus \boldsymbol{\Phi}(\boldsymbol{q}_{\text{prv}}))/T \approx \boldsymbol{J}(\boldsymbol{q}_{\text{prv}})\boldsymbol{u} \tag{110}$$

$$\boldsymbol{\Phi}(\boldsymbol{q}) \approx \boldsymbol{\Phi}(\boldsymbol{q}_{\text{prv}}) \oplus T\boldsymbol{J}(\boldsymbol{q}_{\text{prv}})\boldsymbol{u} \tag{111}$$

if $T > 0$ is small enough.

Appendix B
Proofs of Propositions in Section II-B

In order to provide a proof of Theorem 1, we here introduce the following lemma.

Lemma 1: The following statement holds true:

$$\operatorname*{arglexmin}_{\boldsymbol{\xi}\in\mathbb{R}^n} \{\|\boldsymbol{\Sigma}\boldsymbol{\xi} - \boldsymbol{\beta}\|^2, \|\boldsymbol{\xi}\|^2\} = \boldsymbol{\Sigma}^+\boldsymbol{\beta} \tag{112}$$

where $\boldsymbol{\Sigma} \in \mathbb{R}^{m\times n}$ is a rectangular diagonal matrix with nonnegative diagonal elements and $\boldsymbol{\beta} \in \mathbb{R}^m$ is a vector.

Proof: Because of the property of $\boldsymbol{\Sigma}$, we have the following:

$$\|\boldsymbol{\Sigma}\boldsymbol{\xi} - \boldsymbol{\beta}\|^2 = \sum_{i=1}^{\min(m,n)} (\sigma_i\xi_i - \beta_i)^2 \tag{113}$$

where σ_i is the ith diagonal element of $\boldsymbol{\Sigma}$ and ξ_i and β_i are the ith elements of $\boldsymbol{\beta}$ and $\boldsymbol{\xi}$, respectively. Let $\mathcal{I} \triangleq \{i \in \{1, \dots, \min(m,n)\} \mid \sigma_i > 0\}$. Then, $\|\boldsymbol{\Sigma}\boldsymbol{\xi} - \boldsymbol{\beta}\|^2$ takes its minimum $\sum_{i\notin\mathcal{I}} \beta_i^2$ if $\xi_i = \beta_i/\sigma_i$ for all $i \in \mathcal{I}$. The other elements, ξ_i with $i \notin \mathcal{I}$, should be zero to minimize $\|\boldsymbol{\xi}\|$. Therefore, the left-hand side of (112) is $\boldsymbol{\xi}$ whose elements are

$$\xi_i = \begin{cases} \beta_i/\sigma_i & \text{if } i \in \mathcal{I} \\ 0 & \text{otherwise} \end{cases} \tag{114}$$

which is equivalent to $\boldsymbol{\Sigma}^+\boldsymbol{\beta}$. ■

Based on this Lemma 1, we can prove Theorem 1 as follows.

Proof of Theorem 1: It is known that $\boldsymbol{A}$ can be decomposed into the form of $\boldsymbol{A} = \boldsymbol{U}\boldsymbol{\Sigma}\boldsymbol{V}^T$ where $\boldsymbol{U} \in \mathbb{R}^{m\times m}$ and $\boldsymbol{V} \in \mathbb{R}^{n\times n}$ are orthogonal matrices and $\boldsymbol{\Sigma} \in \mathbb{R}^{m\times n}$ is a rectangular diagonal matrix with nonnegative diagonal elements. Therefore, the left-hand side (lhs) and the right-hand side (rhs) of (10) can be connected as follows:

$$\begin{aligned} \text{lhs of (10)} &= \operatorname*{arglexmin}_{\boldsymbol{x}\in\mathbb{R}^n} \{\|\boldsymbol{U}\boldsymbol{\Sigma}\boldsymbol{V}^T\boldsymbol{x} - \boldsymbol{b}\|^2, \|\boldsymbol{x}\|^2\} \\ &= \boldsymbol{V} \operatorname*{arglexmin}_{\boldsymbol{V}^T\boldsymbol{x}\in\mathbb{R}^n} \{\|\boldsymbol{\Sigma}\boldsymbol{V}^T\boldsymbol{x} - \boldsymbol{U}^T\boldsymbol{b}\|^2, \|\boldsymbol{V}^T\boldsymbol{x}\|^2\} \\ &= \boldsymbol{V}\boldsymbol{\Sigma}^+(\boldsymbol{U}^T\boldsymbol{b}) = \boldsymbol{A}^+\boldsymbol{b} = \text{rhs of (10)}. \end{aligned} \tag{115}$$

Here, we used Lemma 1 by substituting $\boldsymbol{\beta} = \boldsymbol{U}^T\boldsymbol{b}$ and $\boldsymbol{\xi} = \boldsymbol{V}^T\boldsymbol{A}$, and also used the fact that $\|\boldsymbol{U}\boldsymbol{x}\| = \|\boldsymbol{x}\|$ is satisfied for an arbitrary orthogonal matrix $\boldsymbol{U}$. ■

Likewise, a proof of Corollary 1 can be given as follows.

Proof of Corollary 1: The the left-hand side (lhs) and the right-hand side (rhs) of (11) can be connected as follows:

$$\begin{aligned} &\text{lhs of (11)} \\ &= \operatorname*{arglexmin}_{\boldsymbol{C}^{-1}(\boldsymbol{\xi}+\boldsymbol{d})\in\mathbb{R}^n} \{\|\boldsymbol{A}\boldsymbol{C}^{-1}(\boldsymbol{\xi} + \boldsymbol{d}) - \boldsymbol{b}\|^2, \|\boldsymbol{\xi}\|^2\} \\ &= \boldsymbol{C}^{-1} \operatorname*{arglexmin}_{\boldsymbol{\xi}\in\mathbb{R}^n} \{\|\boldsymbol{A}\boldsymbol{C}^{-1}\boldsymbol{\xi} - (\boldsymbol{b} - \boldsymbol{A}\boldsymbol{C}^{-1}\boldsymbol{d})\|^2, \|\boldsymbol{\xi}\|^2\} \end{aligned}$$

$$
\begin{aligned}
&+ \boldsymbol{C}^{-1}\boldsymbol{d} \\
&= \boldsymbol{C}^{-1}(\boldsymbol{A}\boldsymbol{C}^{-1})^{+}(\boldsymbol{b} - \boldsymbol{A}\boldsymbol{C}^{-1}\boldsymbol{d}) + \boldsymbol{C}^{-1}\boldsymbol{d} \\
&= \text{rhs of (11)}. \qquad (116)
\end{aligned}
$$

In the first line, we used $\boldsymbol{x} = \boldsymbol{C}^{-1}(\boldsymbol{\xi} + \boldsymbol{d})$ where $\boldsymbol{\xi} = \boldsymbol{C}\boldsymbol{x} - \boldsymbol{d}$. The equivalence between the second line and the third line is from Theorem 1. ■

Appendix C
Differentiation of $\boldsymbol{J}^{\#}$

This appendix section derives $d(\boldsymbol{J}^{\#})/dt$ in a similar manner to [41]. As mentioned in the Lemma of [41], if a matrix $\boldsymbol{E}$ satisfies $\boldsymbol{E}\boldsymbol{E} = \boldsymbol{E}$, it satisfies $\boldsymbol{E}\dot{\boldsymbol{E}}\boldsymbol{E} = \boldsymbol{O}$, which can be easily shown by noting $\boldsymbol{E}\dot{\boldsymbol{E}} = \boldsymbol{E}(\boldsymbol{E}\dot{\boldsymbol{E}} + \dot{\boldsymbol{E}}\boldsymbol{E}) = \boldsymbol{E}\dot{\boldsymbol{E}} + \boldsymbol{E}\dot{\boldsymbol{E}}\boldsymbol{E}$. Because $\boldsymbol{J}\boldsymbol{J}^{\#}$ and $\boldsymbol{J}^{\#}\boldsymbol{J}$ satisfy this condition, they satisfy the following:

$$\boldsymbol{J}^{\#}\boldsymbol{J}\left(d(\boldsymbol{J}^{\#}\boldsymbol{J})/dt\right)\boldsymbol{J}^{\#}\boldsymbol{J} = \boldsymbol{O}_{n\times n} \qquad (117)$$

$$\boldsymbol{J}\boldsymbol{J}^{\#}\left(d(\boldsymbol{J}\boldsymbol{J}^{\#})/dt\right)\boldsymbol{J}\boldsymbol{J}^{\#} = \boldsymbol{O}_{6\times 6} \qquad (118)$$

which leads to

$$\boldsymbol{J}^{\#}\boldsymbol{J}\boldsymbol{M}^{-1}\left(d(\boldsymbol{J}^{T}\boldsymbol{J}^{\#T})/dt\right)\boldsymbol{M}\boldsymbol{J}^{\#}\boldsymbol{J} = \boldsymbol{O}_{n\times n} \qquad (119)$$

$$\boldsymbol{J}\boldsymbol{J}^{\#}\boldsymbol{M}_{\mathrm{T}}^{-1}\left(d(\boldsymbol{J}^{\#T}\boldsymbol{J}^{T})/dt\right)\boldsymbol{M}_{\mathrm{T}}\boldsymbol{J}\boldsymbol{J}^{\#} = \boldsymbol{O}_{6\times 6}. \qquad (120)$$

Let $\boldsymbol{Z} \triangleq d\boldsymbol{J}^{\#}/dt$. Then, the above-mentioned leads to

$$\boldsymbol{M}^{-1}\boldsymbol{J}^{T}\boldsymbol{Z}^{T}\boldsymbol{M}\boldsymbol{J}^{\#} = -\boldsymbol{M}^{-1}\boldsymbol{J}^{T}\boldsymbol{J}^{\#T}\boldsymbol{H}^{T}\boldsymbol{J}^{\#T}\boldsymbol{M}\boldsymbol{J}^{\#} \qquad (121)$$

$$\boldsymbol{J}^{\#}\boldsymbol{M}_{\mathrm{T}}^{-1}\boldsymbol{Z}^{T}\boldsymbol{J}^{T}\boldsymbol{M}_{\mathrm{T}} = -\boldsymbol{J}^{\#}\boldsymbol{M}_{\mathrm{T}}^{-1}\boldsymbol{J}^{\#T}\boldsymbol{H}^{T}\boldsymbol{J}^{\#T}\boldsymbol{J}^{T}\boldsymbol{M}_{\mathrm{T}}. \qquad (122)$$

Differentiating (51a), (51d), and (51c) yields the following:

$$\boldsymbol{Z} = \boldsymbol{J}^{\#}\boldsymbol{H}\boldsymbol{J}^{\#} + \boldsymbol{Z}\boldsymbol{J}\boldsymbol{J}^{\#} + \boldsymbol{J}^{\#}\boldsymbol{J}\boldsymbol{Z} \qquad (123)$$

$$\boldsymbol{Z}\boldsymbol{J} + \boldsymbol{J}^{\#}\boldsymbol{H} = \boldsymbol{M}^{-1}(\boldsymbol{J}^{T}\boldsymbol{Z}^{T} + \boldsymbol{H}^{T}\boldsymbol{J}^{\#T})\boldsymbol{M} \qquad (124)$$

$$\boldsymbol{J}\boldsymbol{Z} + \boldsymbol{H}\boldsymbol{J}^{\#} = \boldsymbol{M}_{\mathrm{T}}^{-1}(\boldsymbol{Z}^{T}\boldsymbol{J}^{T} + \boldsymbol{J}^{\#T}\boldsymbol{H}^{T})\boldsymbol{M}_{\mathrm{T}}. \qquad (125)$$

Substituting (124) and (125) into (123) leads to the following:

$$
\begin{aligned}
\boldsymbol{Z} = &-\boldsymbol{J}^{\#}\boldsymbol{H}\boldsymbol{J}^{\#} + \boldsymbol{M}^{-1}(\boldsymbol{J}^{T}\boldsymbol{Z}^{T} + \boldsymbol{H}^{T}\boldsymbol{J}^{\#T})\boldsymbol{M}\boldsymbol{J}^{\#} \\
&+ \boldsymbol{J}^{\#}\boldsymbol{M}_{\mathrm{T}}^{-1}(\boldsymbol{Z}^{T}\boldsymbol{J}^{T} + \boldsymbol{J}^{\#T}\boldsymbol{H}^{T})\boldsymbol{M}_{\mathrm{T}}. \qquad (126)
\end{aligned}
$$

By substituting (121) and (122) into (126), one obtains the following:

$$
\begin{aligned}
\frac{d\boldsymbol{J}^{\#}}{dt} = &-\boldsymbol{J}^{\#}\boldsymbol{H}\boldsymbol{J}^{\#} + (\boldsymbol{I} - \boldsymbol{J}^{\#}\boldsymbol{J})\boldsymbol{M}^{-1}\boldsymbol{H}^{T}\boldsymbol{J}^{\#T}\boldsymbol{M}\boldsymbol{J}^{\#} \\
&+ \boldsymbol{J}^{\#}\boldsymbol{M}_{\mathrm{T}}^{-1}\boldsymbol{J}^{\#T}\boldsymbol{H}^{T}\boldsymbol{M}_{\mathrm{T}}(\boldsymbol{I} - \boldsymbol{J}\boldsymbol{J}^{\#}) \qquad (127)
\end{aligned}
$$

which also leads to the following:

$$
\begin{aligned}
\frac{d\boldsymbol{J}^{\#}\boldsymbol{J}}{dt} = &\boldsymbol{J}^{\#}\boldsymbol{H}(\boldsymbol{I}_n - \boldsymbol{J}^{\#}\boldsymbol{J}) \\
&+ (\boldsymbol{I}_n - \boldsymbol{J}^{\#}\boldsymbol{J})\boldsymbol{M}^{-1}\boldsymbol{H}^{T}\boldsymbol{J}^{\#T}\boldsymbol{M}. \qquad (128)
\end{aligned}
$$

References

[1] A. Peer and M. Buss, "A new admittance-type haptic interface for bimanual manipulations," *IEEE/ASME Trans. Mechatron.*, vol. 13, no. 4, pp. 416–428, Aug. 2008.

[2] R. Q. Van Der Linde and P. Lammertse, "HapticMaster–A generic force controlled robot for human interaction," *Ind. Robot*, vol. 30, no. 6, pp. 515–524, 2003.

[3] E. G. Kaigom and J. Roßmann, "Physics-based simulation for manual robot guidance–An eRobotics approach," *Robot. Comput.-Integr. Manuf.*, vol. 43, pp. 155–163, 2017.

[4] H. Chen, W. Xu, W. Guo, and X. Sheng, "Variable admittance control using velocity-curvature patterns to enhance physical human-robot interaction," *IEEE Robot. Automat. Lett.*, vol. 9, no. 6, pp. 5054–5061, Jun. 2024.

[5] A. Campeau-Lecours, M. J.-D. Otis, and C. Gosselin, "Modeling of physical human-robot interaction: Admittance controllers applied to intelligent assist devices with large payload," *Int. J. Adv. Robotic Syst.*, vol. 13, no. 5, pp. 1–12, 2016.

[6] I. Yoon, M. Na, and J.-B. Song, "Assembly of low-stiffness parts through admittance control with adaptive stiffness," *Robot. Comput.- Integr. Manuf.*, vol. 86, 2024, Art. no. 102678.

[7] A. Morbi, M. Ahmadi, A. D. C. Chan, and R. Langlois, "Stability-guaranteed assist-as-needed controller for powered orthoses," *IEEE Trans. Control Syst. Technol.*, vol. 22, no. 2, pp. 745–752, Mar. 2014.

[8] A. Morbi and M. Ahmadi, "Safely rendering small impedance in admittance-controlled haptic devices," *IEEE/ASME Trans. Mechatron.*, vol. 21, no. 3, pp. 1272–1280, Jun. 2016.

[9] T. Osa, S. Uchida, N. Sugita, and M. Mitsuishi, "Hybrid rate-admittance control with force reflection for safe teleoperated surgery," *IEEE/ASME Trans. Mechatron.*, vol. 20, no. 5, pp. 2379–2390, Oct. 2015.

[10] R. Kikuuwe, "Torque-bounded admittance control realized by a set-valued algebraic feedback," *IEEE Trans. Robot.*, vol. 35, no. 5, pp. 1136–1149, Oct. 2019.

[11] V. Kurtz, P. M. Wensing, and H. Lin, "Control barrier functions for singularity avoidance in passivity-based manipulator control," in *Proc. IEEE Conf. Decis. Control*, 2021, pp. 6125–6130.

[12] F. Dimeas, V. C. Moulianitis, and N. Aspragathos, "Manipulator performance constraints in human-robot cooperation," *Robot. Comput.- Integr. Manuf.*, vol. 50, pp. 222–233, 2018.

[13] J. Šifrer and T. Petrič, "Leveraging environmental contact and sensor feedback for precision in robotic manipulation," *Sensors*, vol. 24, 2024, Art. no. 7006.

[14] M. G. Carmichael, D. Liu, and K. J. Waldron, "A framework for singularity-robust manipulator control during physical human-robot interaction," *Int. J. Robot. Res.*, vol. 36, no. 5–7, pp. 861–876, 2017.

[15] A. Colomé and C. Torras, "Closed-loop inverse kinematics for redundant robots: Comparative assessment and two enhancements," *IEEE/ASME Trans. Mechatron.*, vol. 20, no. 2, pp. 944–955, Apr. 2015.

[16] H.-J. Kang and R. A. Freeman, "Null space damping method for local joint torque optimization of redundant manipulators," *J. Robotic Syst.*, vol. 10, no. 2, pp. 249–270, 1992.

[17] H. Sadeghian, L. Villani, M. Keshmiri, and B. Siciliano, "Task-space control of robot manipulators with null-space compliance," *IEEE Trans. Robot.*, vol. 30, no. 2, pp. 493–506, Apr. 2014.

[18] A. Wahrburg, J. Boes, B. Matthias, F. Dai, and H. Ding, "Sensorless null-space admittance control for redundant manipulators," in *Proc. Int. Symp. Robot.*, 2016, pp. 1–7.

[19] M. P. A. Fonseca, B. V. Adorno, and P. Fraisse, "Coupled task-space admittance controller using dual quaternion logarithmic mapping," *IEEE Robot. Automat. Lett.*, vol. 5, no. 4, pp. 6057–6064, Oct. 2020.

[20] L. Zhang, H. Yu, and X. Cui, "Impedance-based null-space control of redundant torque-controlled robot," *Ind. Robots*, vol. 51, no. 5, pp. 799–808, 2024.

[21] M. Benallegue et al., "On compliance and safety with torque-control for robots with high reduction gears and no joint-torque feedback," in *Proc. IEEE/RSJ Int. Conf. Intell. Robots Syst.*, 2021, pp. 6262–6269.

[22] J. Hermus, J. Lachner, D. Verdi, and N. Hogan, "Exploiting redundancy to facilitate physical interaction," *IEEE Trans. Robot.*, vol. 38, no. 1, pp. 599–615, Feb. 2022.

[23] F. Benzi and C. Secchi, "A null-space based approach for a safe and effective human-robot collaboration," in *Proc. IEEE/RSJ Int. Conf. Intell. Robots Syst.*, 2022, pp. 3694–3700.

[24] V. Acary and B. Brogliato, *Numerical Methods for Nonsmooth Dynamical Systems: Applications in Mechanics and Electronics*, (Ser. Lecture Notes in Applied and Computational Mechanics), vol. 35. Berlin, Germany: Springer, 2008.

[25] B. Brogliato, *Nonsmooth Mechanics: Models, Dynamics and Control*, 3rd ed. Berlin, Germany: Springer, 2016.
[26] R. Kikuuwe and B. Brogliato, "A new representation of systems with frictional unilateral constraints and its Baumgarte-like relaxation," *Multibody System Dyn.*, vol. 39, no. 3, pp. 267–290, 2017.
[27] Y. Wang, R. Wang, H. Meng, and B. Zhang, "An investigation of the dynamic performance of lateral inerter-based vibration isolator with geometrical nonlinearity," *Arch. Appl. Mechan.*, vol. 89, pp. 1953–1972, 2019.
[28] J. Angeles, *Fundamentals of Robotic Mechanical Systems*. Berlin, Germany: Springer, 2014.
[29] J.-Y. Rhee and B. Lee, "Analytical method for differentiation of robot Jacobian," *Electron. Lett.*, vol. 53, no. 6, pp. 386–387, 2017.
[30] D. Di Vito, C. Natale, and G. Antonelli, "A comparison of damped least squares algorithms for inverse kinematics of robot manipulators," in *IFAC PapersOnLine*, vol. 50, 2017, pp. 6869–6874.
[31] A. Dietrich, C. Ott, and A. Albu-Schäffer, "An overview of null space projections for redundant, torque-controlled robots," *Int. J. Robot. Res.*, vol. 34, no. 11, pp. 1385–1400, 2015.
[32] J. G. Ziegler and N. B. Nichols, "Optimum settings for automatic controllers," *Trans. ASME*, vol. 64, pp. 759–768, 1942.
[33] O. Khatib, "Inertial properties in robotic manipulation: An object-level framework," *Int. J. Robot. Res.*, vol. 13, no. 1, pp. 19–36, 1995.
[34] R. Featherstone and O. Khatib, "Load independence of the dynamically consistent inverse of the Jacobian matrix," *Int. J. Robot. Res.*, vol. 16, no. 2, pp. 168–170, 1997.
[35] Kinova Inc., "User guide: KINOVA Gen3 Ultra lightweight robot," 2022. [Online]. Available: https://www.kinovarobotics.com/uploads/User-Guide-Gen3-R07.pdf
[36] M. P. A. Fonseca, B. V. Adorno, and P. Fraisse, "Task-space admittance controller with adaptive inertia matrix conditioning," *J. Intell. Robotic Syst.*, vol. 101, 2021, Art. no. 41.
[37] Y. Michel, Y. Abdelhalem, and G. Cheng, "Passivity-based teleoperation with variable rotational impedance control," *IEEE Robot. Automat. Lett.*, vol. 9, no. 12, pp. 11658–11665, Dec. 2024.
[38] J. Solà, "Quaternion kinematics for the error-state Kalman filter," 2017, *arXiv:1711.02508v1*.
[39] N. Ramuzat, O. Stasse, and S. Boria, "Benchmarking whole-body controllers on the TALOS humanoid robot," *Front. Robot. AI*, vol. 9, 2022, Art. no. 826491.
[40] B. Wingo, A. S. Sathya, S. Caron, S. Hutchinson, and J. Carpentier, "Linear-time differential inverse kinematics: An augmented Lagrangian perspective," in *Proc. Robot.: Sci. Syst.*, 2024, Art. no. 110.
[41] J. Decell and P. Henry, "On the derivative of the generalized inverse of a matrix," *Linear Multilinear Algebra*, vol. 1, pp. 357–359, 1974.

Ryo Kikuuwe (Member, IEEE) received the B.S., M.S., and Ph.D. (Eng.) degrees in mechanical engineering from Kyoto University, Kyoto, Japan, in 1998, 2000, and 2003, respectively.

From 2003 to 2007, he was an Endowed-Chair Research Associate with the Nagoya Institute of Technology, Nagoya, Japan. From 2007 to 2017, he was an Associate Professor with the Department of Mechanical Engineering, Kyushu University, Fukuoka, Japan. From 2014 to 2015, he was a Visiting Researcher with Inria Grenoble Rhône-Alpes, Saint-Ismier, France. He is currently a Full Professor with the Graduate School of Advanced Science and Engineering, Hiroshima University, Hiroshima, Japan. His research interests include force control of robot manipulators, control and modeling of hydraulic systems, and engineering applications of differential inclusions.

Dr. Kikuuwe is a Member of the Robotics Society of Japan, the Japan Society of Mechanical Engineers, and the Society of Instrument and Control Engineers (Japan). He was a recipient of the Best Paper Award of Advanced Robotics in 2013 and the Young Investigator Excellence Award from the Robotics Society of Japan in 2005.